






Solid stress impairs lymphocyte infiltration into lymph-node metastases

Dennis Jones^{1,2,3} , Zixiong Wang³, Ivy X. Chen^{1,2}, Sue Zhang⁴, Rohin Banerji⁴, Pin-Ji Lei^{1,2}, Hengbo Zhou^{1,2}, Victoria Xiao¹, Cecilia Kwong¹, Jan Willem M. van Wijnbergen^{1,2}, Ethel R. Pereira^{1,2}, Benjamin J. Vakoc^{2,5}, Peigen Huang^{1,2}, Hadi T. Nia⁴  and Timothy P. Padera^{1,2} 

Strong and durable anticancer immune responses are associated with the generation of activated cancer-specific T cells in the draining lymph nodes. However, cancer cells can colonize lymph nodes and drive tumour progression. Here, we show that lymphocytes fail to penetrate metastatic lesions in lymph nodes. In tissue from patients with breast, colon, and head and neck cancers, as well as in mice with spontaneously developing breast-cancer lymph-node metastases, we found that lymphocyte exclusion from nodal lesions is associated with the presence of solid stress caused by lesion growth, that solid stress induces reductions in the number of functional high endothelial venules in the nodes, and that relieving solid stress in the mice increased the presence of lymphocytes in lymph-node lesions by about 15-fold. Solid-stress-mediated impairment of lymphocyte infiltration into lymph-node metastases suggests a therapeutic route for overcoming T-cell exclusion during immunotherapy.

Lymph node (LN) metastases lead to poor overall prognosis, probably due to the metastatic potential of primary tumour cells, the contribution of LN metastases to distant metastases and survival advantages that cancer cells gain from lymph^{1–6}. The spatial organization of lymph nodes (LNs) facilitates the interaction of antigens and antigen-presenting cells with T cells. Tumour-draining LNs (TDLNs) have recently been shown to be critical for the generation of anti-tumour T-cell responses and for the response to immunotherapy^{7–14}. Paradoxically, it is these organs, which should be generating antitumour immunity, that are frequently the first site of spread and growth of metastatic cancers.

Exosomes, growth factors and cytokines precondition TDLNs to enable cancer cell colonization and growth before the arrival of cancer cells^{15,16}. Part of this preconditioning includes causing immunosuppression within premetastatic LNs by the expansion of regulatory T cells as well as the accumulation of immature dendritic cells and immunosuppressive proteins that promote immune tolerance¹⁷. These changes ultimately limit the number of functional cancer-specific T cells that are available to eliminate the cancer. Breaking or bypassing immune tolerance in non-cancer-bearing LNs can expand cancer-specific T cells and attenuate primary tumour growth^{18,19}.

The mechanisms of how cancer cells evade immune surveillance once in the LNs are not well understood. Past studies have shown that the invasion of cancer cells into LNs enhances local and systemic immune suppression^{10,20–22}. Given the importance of the LN architecture in regulating immune function, surprisingly little is known about the effect of cancer growth on LN structure and, in turn, the lack of anticancer immune responses.

Solid stresses—mechanical forces generated by the growth of cancer cells and extracellular matrix²³—can perturb tissue architecture and compress blood and lymphatic vessels in primary tumours^{24,25}.

We recently measured elevated solid stresses in metastatic LNs²⁶, but their consequences in this immune organ are unknown.

In this Article, we used models of spontaneous mouse lymphatic metastases to investigate the lack of immune responses in metastatic LNs. We discovered that solid stresses can remodel high endothelial venules (HEVs) in metastatic LNs, which leads to the exclusion of lymphocytes in metastatic lesions. Our data suggest that controlling solid stresses in LNs may enhance anticancer immunity by improving T-cell trafficking into LN metastases.

Results

Exclusion of lymphocytes from human LN metastases. Using immunofluorescence (IF) staining, we evaluated lymphocyte infiltration into LN metastases of patients with breast cancer, head and neck cancer and colon cancer, and found a paucity of both B and T cells (Fig. 1a–d), including CD8⁺ T cells (Extended Data Fig. 1a,b), within metastatic lesions, even though the surrounding LN tissue contained many lymphocytes. In contrast to the exclusion of lymphocytes, macrophages were abundant in metastatic lesions from patient LNs (Fig. 1e,f), indicating that lymphocytes are selectively excluded.

Exclusion of lymphocytes from mouse LN metastases. To mechanistically study this process, we examined whether spontaneous mouse LN metastasis demonstrated a similar lack of lymphocytic infiltration. We grew the well-differentiated oestrogen-receptor-(ER)-positive mammary adenocarcinoma MCA-P1362 (MCA) cell line (originating in our laboratory) and the poorly differentiated 4T1 triple-negative breast cancer cells in the mammary fat pad of immunocompetent, syngeneic mice and allowed them to spontaneously metastasize to the draining LN (Extended Data Fig. 2a). Consistent with LN metastases from patients, analysis of the spatial distribution of immune cells in 4T1 and MCA LN metastatic lesions

¹Edwin L. Steele Laboratories for Tumor Biology, Department of Radiation Oncology, Massachusetts General Hospital, Boston, MA, USA. ²Harvard Medical School, Boston, MA, USA. ³Department of Pathology and Laboratory Medicine, Boston University School of Medicine, Boston, MA, USA. ⁴Department of Biomedical Engineering, Boston University, Boston, MA, USA. ⁵Wellman Center for Photomedicine, Massachusetts General Hospital, Boston, MA, USA.

✉e-mail: djones1@bu.edu; tpadera@steele.mgh.harvard.edu

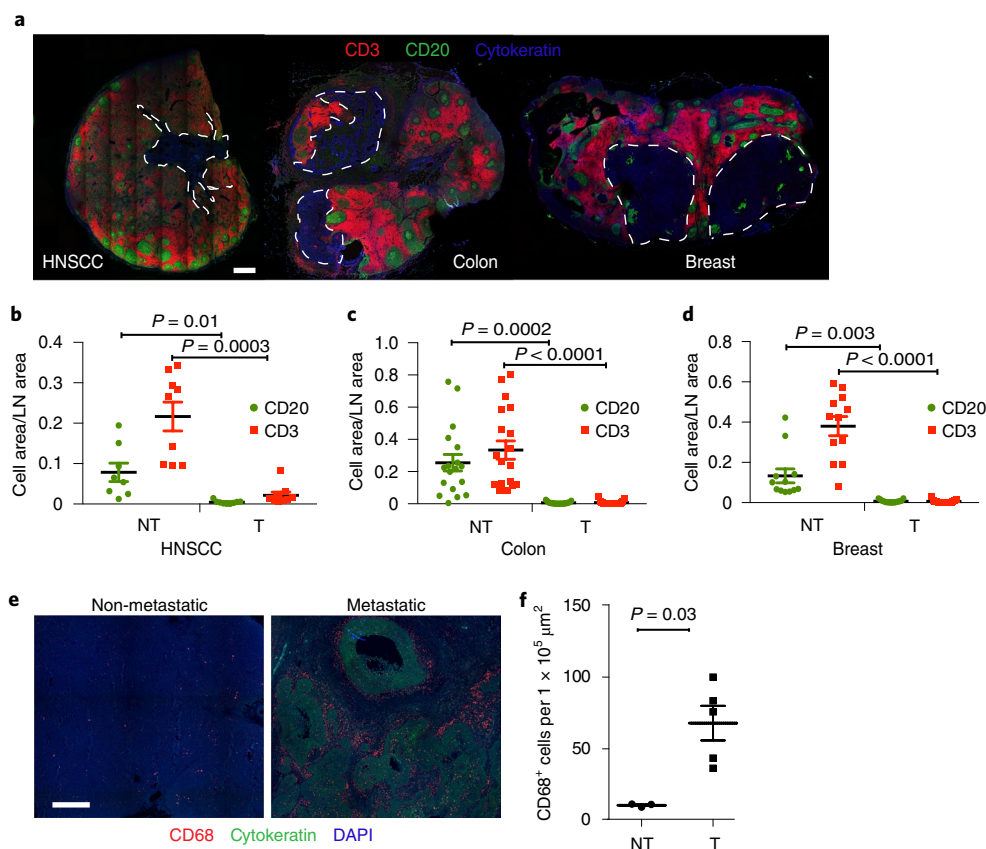


Fig. 1 | Immune evasion by human cancer cells within metastatic LNs. **a**, Representative IF staining of metastatic LNs from patients with head and neck, colon and breast cancer. Scale bar, 1.2 mm. The number of images taken is reflected in the n values for **b–d**. The dashed lines indicate the margin of the LN lesion. **b–d**, Lymphocyte quantification within the non-tumour area (NT) and tumour area (T) of metastatic LNs from patients with head and neck cancer (**b**), colon cancer (**c**) and breast cancer (**d**). $n = 9$ patients with head and neck cancer ($n = 8$ (non-tumour B-cell area), $n = 9$ (non-tumour T-cell area) and $n = 9$ (tumour B- and T-cell area)). T- and B-cell area fraction from $n = 13$ patients with colon cancer was measured ($n = 18$ (non-tumour B-cell area), $n = 19$ (non-tumour T-cell area) and $n = 21$ (tumour B- and T-cell area)). T- and B-cell area fraction from $n = 7$ patients with breast cancer was measured ($n = 12$ (non-tumour B- and T-cell area) and $n = 15$ (tumour B- and T-cell area)). **e**, Representative IF staining of CD68⁺ macrophages (red) in a non-metastatic TDLN and a metastatic LN from a patient with head and neck cancer. Cancer cells are stained green (cytokeratin⁺), and DAPI (blue) stains all nucleated cells. $n = 5$ images taken from $n = 5$ non-metastatic LNs, $n = 5$ images from $n = 5$ metastatic LNs. Scale bar, 500 μm . **f**, Quantification of CD68⁺ macrophages within LN tumour and non-tumour areas from patients with head and neck squamous cell carcinoma (HNSCC). $n = 5$ LNs from $n = 5$ different patients; two of the LNs did not have a non-tumour area. Data are mean \pm s.e.m. For **b–d** and **f**, significance was tested using two-tailed paired Student's t -tests (**b–d**) and an unpaired Student's t -test (**f**).

revealed few lymphocytes (Fig. 2a–d), including CD8⁺ T cells (Extended Data Fig. 1c,d), while macrophages were abundant in metastatic lesions (Fig. 2e,f). As has been previously shown in other tumour models^{27,28}, flow cytometry analysis (Extended Data Fig. 2b) of 4T1-tumour bearing mice showed a greater percentage of B cells from all CD45⁺ cells, with a similar proportional decrease in T cells, compared with tumour-naïve control animals (Extended Data Fig. 2d,e). The total numbers of both B and T cells showed similar trends (Extended Data Fig. 2f,g). Surprisingly, we found no difference in FoxP3⁺ regulatory T cells (Extended Data Fig. 2h), which are expanded in metastatic LNs of patients with breast cancer and inhibit conventional T cell proliferation²¹. By contrast, an increase in the CD8⁺, but not CD4⁺, T-cell population relative to all CD3⁺ cells was found in metastatic LNs compared with non-metastatic TDLNs (Extended Data Fig. 2i,j). Interestingly, the frequency of CD8⁺granzyme B⁺ T cells (Fig. 2g,h) was also increased within metastatic LNs with large 4T1 lesions, suggesting that cancer-specific T cells were activated as lesions grow. We also identified granzyme B⁺ cells in metastatic LNs of patients with breast cancer (Fig. 2i); however, they were also excluded from the metastatic lesions.

Primary 4T1 tumours showed a T-cell infiltrate, but few B cells (Extended Data Fig. 3a,b).

Blocking lymphocyte exit from LNs does not increase the presence of lymphocytes in nodal lesions.

To determine whether cancer cells promote lymphocyte exit from metastatic LNs, we treated animals with FTY720, a sphingosine-1-phosphate receptor 1 ligand that blocks lymphocyte extravasation from secondary lymphoid organs. Treatment was initiated 7 d after primary tumour implantation and continued daily for 3 weeks (Fig. 3a). Then, 14 d after tumour implantation, primary tumours were resected to prevent them from growing larger than the allowable size and permitting LN metastases to continue to grow for an additional 14 d under FTY720 treatment. No differences were detected in the rate of T-cell proliferation between the vehicle- and FTY720-treated groups (Extended Data Fig. 3c). Furthermore, no proliferating T cells were identified in metastatic lesions in either treatment group. Compared to animals treated with vehicle control, no statistically significant difference was measured in the incidence of LN metastasis, although lung metastasis was significantly increased in animals that were administered FTY720 (Fig. 3b,c). These data also show that FTY720

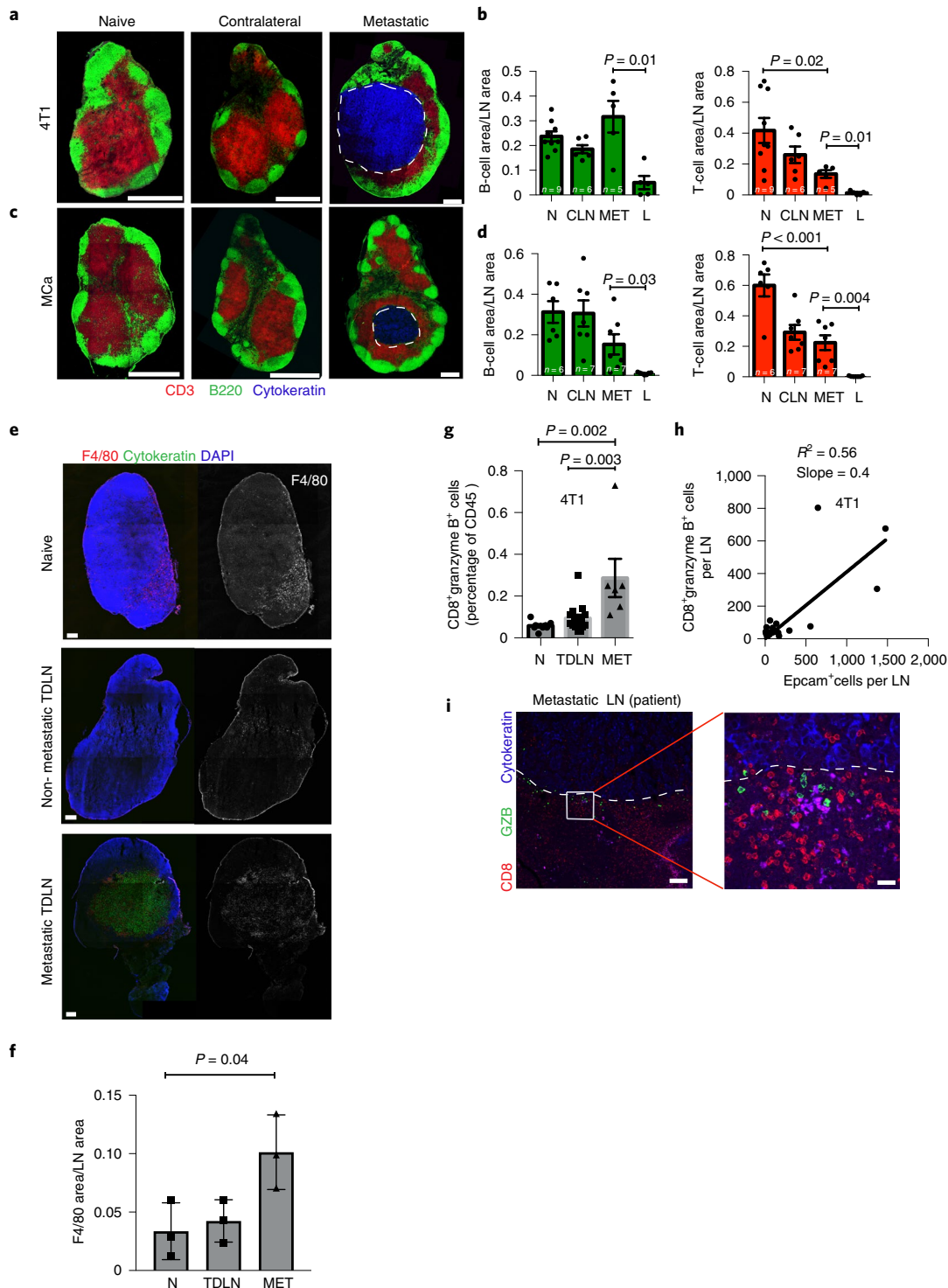


Fig. 2 | Selective exclusion of T cells from LN metastases. **a, c**, Naive, contralateral and metastatic LNs from mice bearing 4T1 (**a**) or MCa (**c**) tumours. Cancer cells (blue), CD3⁺ T cells (red) and B220⁺ B cells (green) are shown. The dashed lines indicate the margin of the LN lesions. Scale bars, 636 μ m. The number of images taken is reflected in the *n* values for **b, d**. **b, d**, Quantification of B- and T-cell area per LN area in naive LNs (N), contralateral LNs (CLN), metastatic LNs (MET) and metastatic lesions within a metastatic LN (L) in the 4T1 (**b**) and MCa (**d**) models. For 4T1: *n* = 9 (naive LNs), *n* = 6 (contralateral LNs), *n* = 5 (metastatic LNs) and *n* = 5 (metastatic lesions within a metastatic LN). For MCa: *n* = 6 (naive LNs), *n* = 7 (contralateral LNs), *n* = 7 (metastatic LNs) and *n* = 7 (metastatic lesions within a metastatic LN). **e**, Representative IF staining (of three in each group) of F4/80⁺ macrophages (red, left; white, right) in naive LNs, non-metastatic TDLNs and metastatic TDLNs from BALB/c mice. Scale bars, 200 μ m. **f**, Quantification of F4/80⁺ macrophages within naive LNs and non-metastatic and metastatic TDLNs. *n* = 3. **g**, The percentage of CD8 T cells expressing granzyme B in naive LNs (N; *n* = 8), TDLNs (*n* = 15) and 4T1 MET LNs (*n* = 6). **h**, Correlation of the absolute counts of granzyme B⁺ CD8 T cells and 4T1 cancer cells in MET LNs. *n* = 21. **i**, Granzyme B staining (GZB, green) in the LN of a patient with breast cancer. *n* = 5 images taken. The dashed line indicates the margin of the LN lesion. Scale bars, 120 μ m (left) and 25 μ m (right). For **b, d, f** and **g**, data are mean \pm s.e.m. Significance was tested using one-way ANOVA with Tukey's honestly significant difference post hoc test.

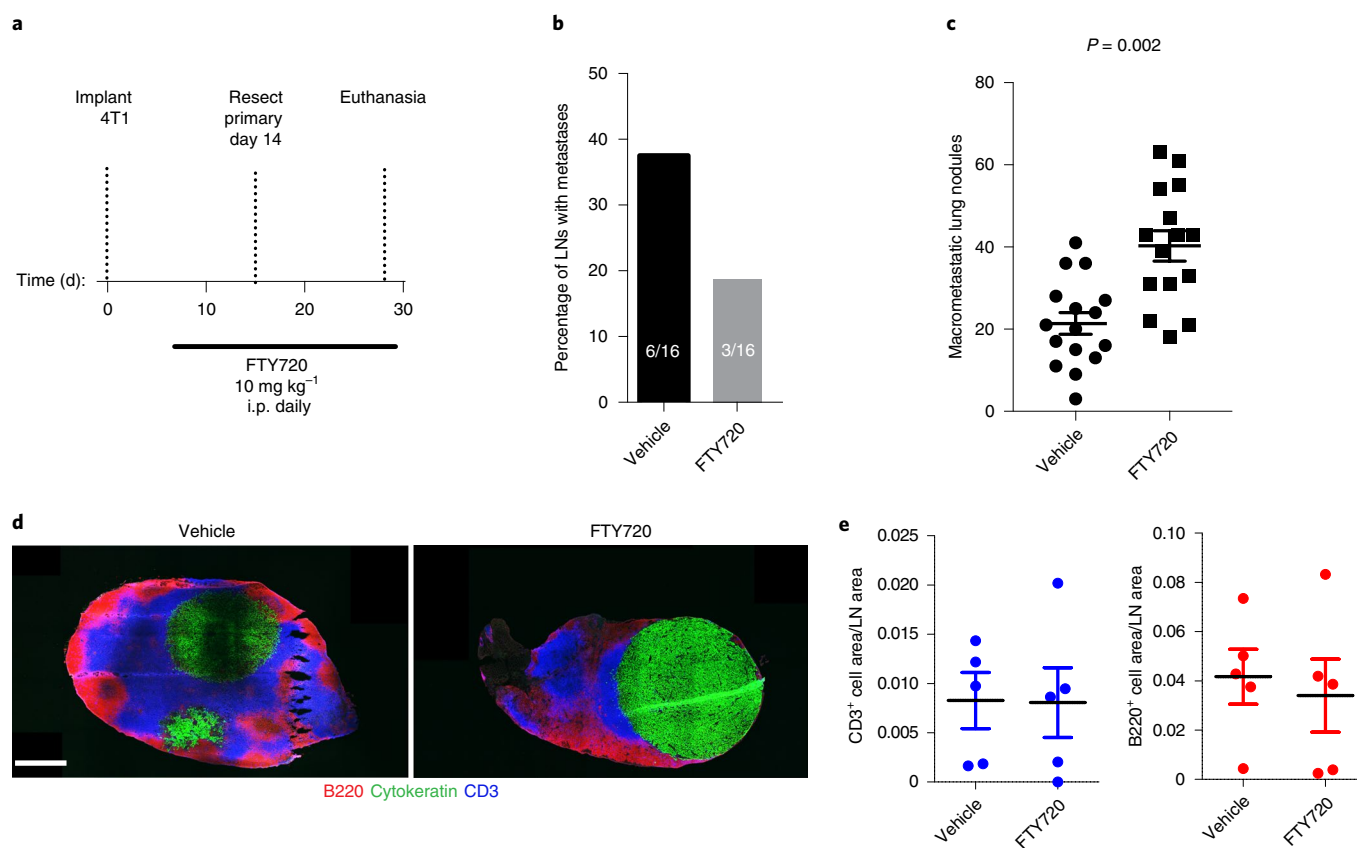


Fig. 3 | Effect of sphingosine-1-phosphate receptor inhibition on metastatic burden. **a**, Schematic of the treatment regimen. **b**, Incidence of metastatic LNs after FTY720 or vehicle treatment, as determined by cytokeratin staining of serial LN sections ($n=16$ per group). The experiment is representative of two biological replicate studies. **c**, Quantification of pulmonary macrometastatic nodules after treatment with FTY720 or vehicle. $n=16$ (vehicle) and $n=5$ (FTY720). **d**, Representative IF staining of T cells (CD3, blue), cancer cells (cytokeratin, green) and B cells (B220, red) in LNs from vehicle- or FTY720-treated animals. Scale bar, 636 μm . $n=5$ images for each group were taken. **e**, Quantification of T-cell (left) and B-cell (right) infiltration of vehicle-treated or FTY720-treated metastatic LNs. For **b**, statistical analysis was performed using a $2 \times 2 \chi^2$ test with Yates correction (no significance was found). For **c** and **e**, significance was tested using two-tailed unpaired Student's *t*-tests. Data are mean \pm s.e.m.

did not increase the presence of lymphocytes in LN metastatic lesions (Fig. 3d,e).

Blocking PD-L1/PD-1 or IDO signalling does not enhance lymphocyte presence in LN lesions. We next hypothesized that the limited presence of T cells within LN metastases may be due to an immunosuppressive microenvironment and focused initially on programmed cell death ligand-1/programmed cell death-1 (PD-L1/PD-1) signalling on the basis of their upregulation in TDLNs (Extended Data Fig. 4a–c). In mice with LN metastasis after primary 4T1 tumours were resected, anti-PD-1 monotherapy provided no overall survival benefit (Extended Data Fig. 4d; $P=0.39$) or reduction in the incidence of LN metastases (Extended Data Fig. 4e). The nodal lesion size and the degree of lymphocytic infiltration were similar to that in mice that were treated with the isotype control (Extended Data Fig. 4f,g). In agreement with clinical findings from patients with melanoma²⁹, the lack of lymphocytes within nodal lesions may explain their resistance to immune checkpoint inhibition. Indoleamine 2,3-dioxygenase (IDO), an enzyme that is involved in tryptophan metabolism that leads to the exclusion of T cells in primary tumours^{30,31}, was found in 4T1 metastatic LNs (Extended Data Fig. 5a). On the basis of the lymphocyte exclusion and the lack of proliferating T cells in nodal lesions, we hypothesized that the production of IDO in metastatic LNs reduced tryptophan availability, which is required for lymphocyte activation

and proliferation³². However, blocking IDO did not reduce the incidence of macrometastatic nodal or lung lesions nor increase lymphocytic infiltration into metastatic lesions in LNs (Extended Data Fig. 5b–g), suggesting that IDO and tryptophan availability do not have a substantial role in limiting T-cell activity in nodal lesions of the 4T1 model.

LN metastases remodel lesion-associated vasculature. Next, we hypothesized that the limited presence of lymphocytes in nodal lesions was due to a specific failure of lymphocyte recruitment to metastatic lesions within LNs. Most circulating naive and central memory lymphocytes enter a LN by extravasating through peripheral node addressin (PNAd)-positive HEVs³³. Previously, we found a lack of angiogenesis in metastatic LNs and a lower vessel density within metastatic lesions compared with the remaining LN tissue³⁴. Thus, we hypothesized that this lack of angiogenesis and associated vascular remodelling also led to a lack of HEVs in metastatic lesions in LNs, which would result in impaired lymphocyte extravasation through HEVs. Compared with the adjacent LN tissue, PNAd⁺ HEVs were significantly reduced within the metastatic lesions in LNs from patients with breast cancer, head and neck cancer and colon cancer (Fig. 4a–d). Similarly, we found significantly fewer HEVs within metastatic lesions of mice bearing MCA or 4T1 breast cancer (Fig. 4e–h). HEV wall thickness was maintained in non-metastatic TDLNs and in the remaining LN tissue of metastatic

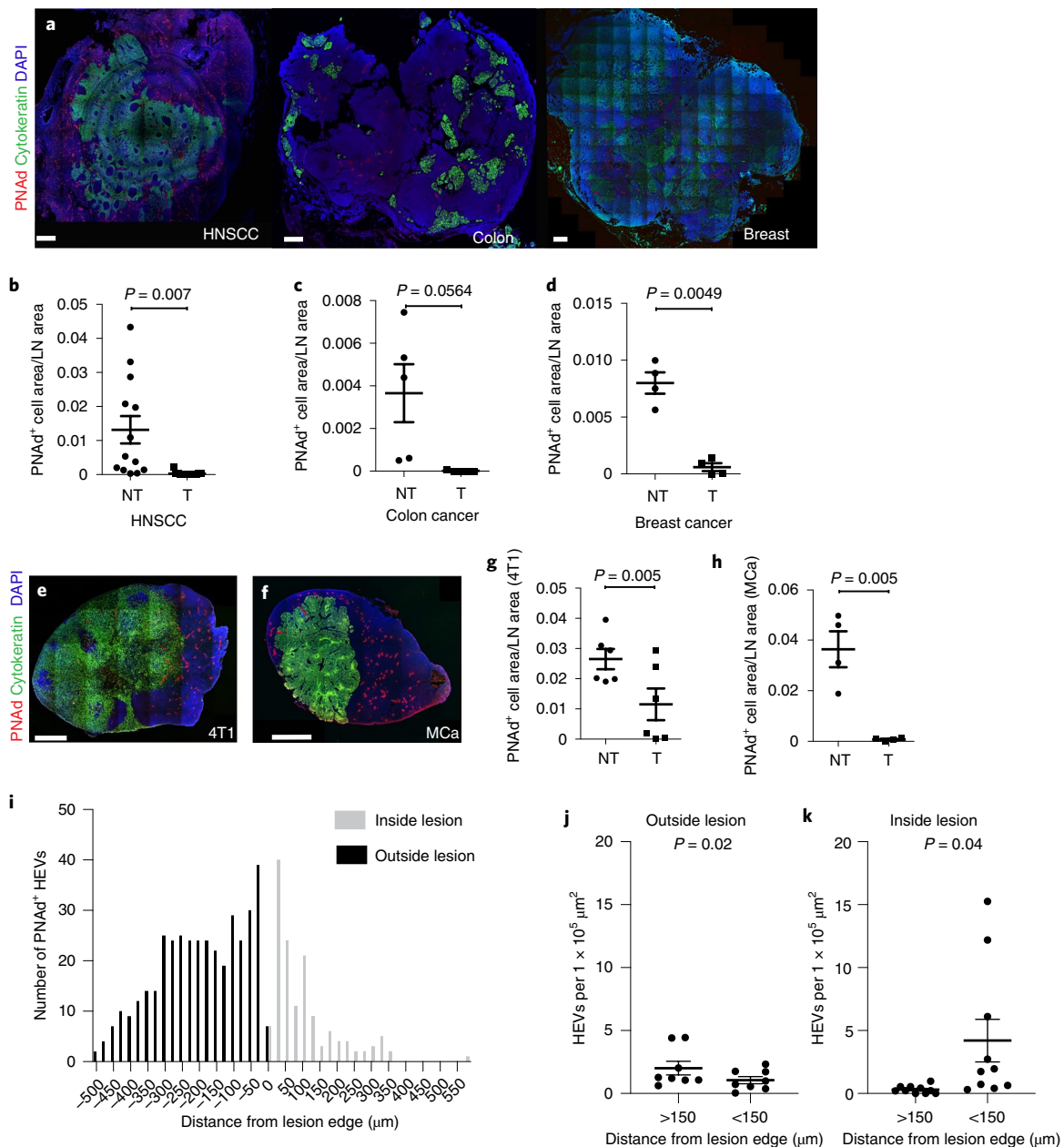


Fig. 4 | Reduced HEVs in metastatic lesions. **a**, Representative IF analysis of PNAAd⁺ HEVs (red) of metastatic LNs from patients with HNSCC, colon cancer and breast cancer. Cancer cells were stained with anti-cytokeratin (green) and DAPI (blue) stains all nucleated cells. Scale bars, 636 μm (HNSCC and breast cancer) and 350 μm (colon cancer). The number of images taken is reflected in the n values for **b-d**. **b-d**, PNAAd quantification of patients with HNSCC ($n=12$) (**b**), colon cancer ($n=5$) (**c**) and breast cancer ($n=4$) (**d**). **e,f**, IF analysis of HEVs (PNAAd⁺; red) in MET LNs from mouse 4T1 (**e**) and MCa (**f**) tumours. Cancer cells were stained with anti-cytokeratin antibodies (green) and DAPI (blue). For **e** and **f**, scale bars, 636 μm . The number of images taken is reflected in the n values for **g** and **h**. **g,h**, PNAAd quantification of 4T1 ($n=6$) (**g**) and MCa ($n=4$) (**h**) LN metastases. **i**, The frequency distribution of the number of HEVs on the basis of the distance from the edge of the metastatic lesion ($x=0$); negative values indicate vessels outside the lesion, and positive values indicate vessels inside the lesion. $n=4$. **j,k**, The number of HEVs per defined area and the distance outside (**j**; $n=7$) and inside (**k**, $n=11$) metastatic lesions. Data are mean \pm s.e.m. Significance was tested using two-tailed paired Student's t -tests.

TDLNs. By contrast, in the few present HEVs in metastatic lesions, the HEVs were thin walled (Extended Data Fig. 6a,b). Furthermore, we measured a steep decline in the number of HEVs that were deep within metastatic lesions ($>150\mu\text{m}$ from the lesion border) compared with HEVs outside lesions (Fig. 4i-k).

LN metastases decrease blood vessel perfusion within lesions. We next investigated how HEVs were compromised within mouse metastatic LNs. To this end, we used optical coherence tomography

(OCT)³⁵ to longitudinally measure functional blood vessels in metastatic LNs using our chronic LN window³⁴. As metastatic lesions progressed, vessel perfusion was decreased within the lesion (Fig. 5a-c; $P < 0.05$), while TDLNs with no detectable cancer cells did not show a decline in vessel perfusion (Extended Data Fig. 7a). We also identified fewer lectin-perfused blood vessels in metastatic lesions relative to non-tumour LN tissue (Extended Data Fig. 7b,c). The reduced perfusion and decreased vessel diameter in large lesions can limit the ability of lymphocytes to enter into these lesions.

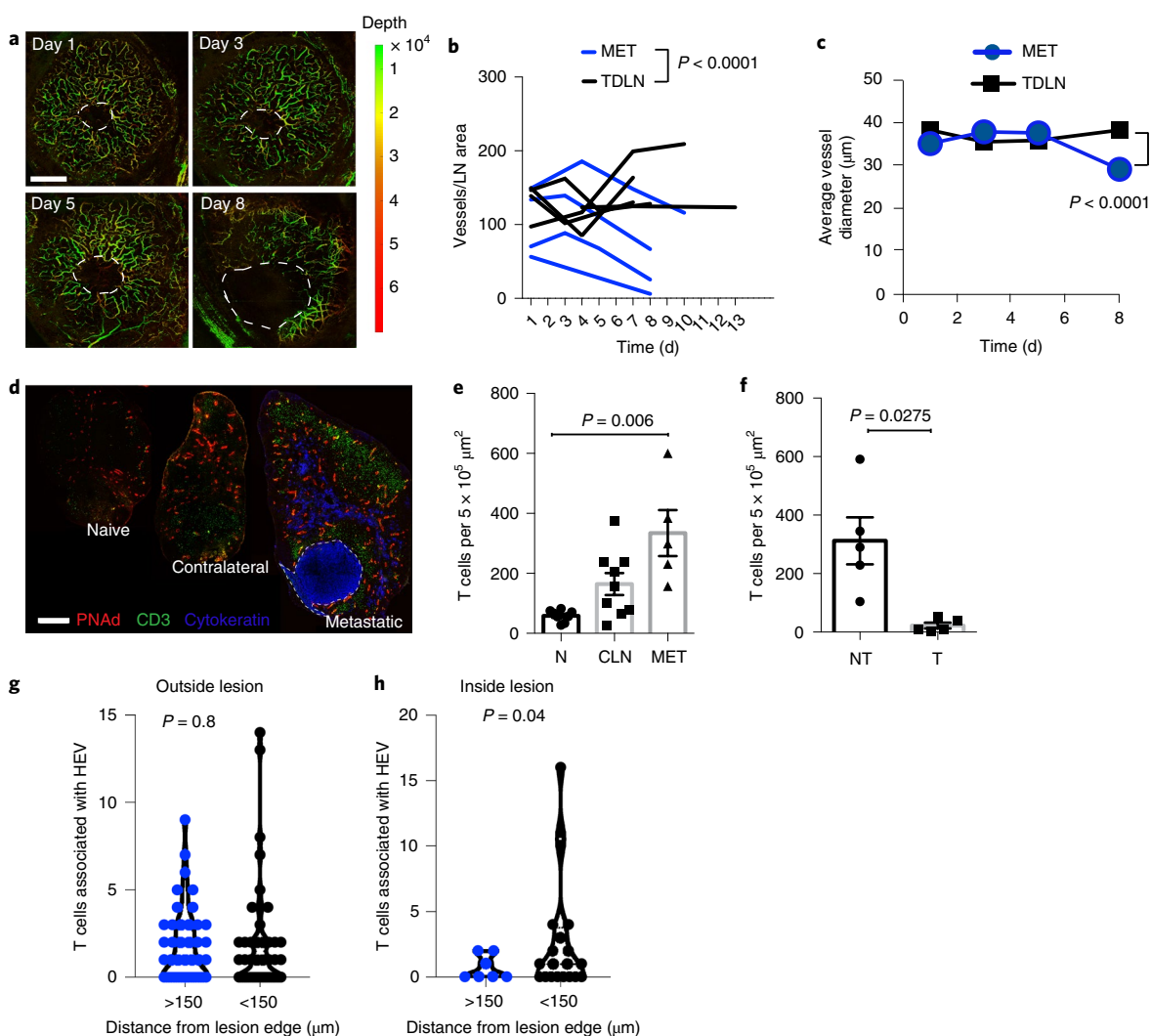


Fig. 5 | Impaired blood vessel function in metastatic lesions. **a**, Doppler OCT image of a metastatic LN on days 1, 3, 5 and 8 after primary tumour (4T1) resection. The depth is denoted by colour: yellow/green (superficial); red (deep). OCT detects vessels up to approximately 1 mm. The dashed lines indicate the margin of the LN lesion. Scale bar, 500 μm . The experiment is representative of four biological replicates. **b**, Quantification of vessels per $5 \times 10^5 \mu\text{m}^2$ in individual non-metastatic (TDLN, $n=5$) and metastatic (MET, $n=4$) LNs from longitudinal imaging by OCT. **c**, Quantification of OCT vessel diameter from metastatic and non-metastatic LNs. The experiment is representative of four biological replicates. **d**, Adoptive transfer of CMFDA-labelled (green) naive T cells into naive or 4T1 tumour-bearing mice 14 d after primary tumour resection (PNAd⁺ HEVs; red) and cancer cells (cytokeratin⁺, blue). Scale bar, 636 μm . **e, f**, Quantification of adoptively transferred T cells entering naive LNs (N, $n=8$), contralateral LNs (CLN, $n=9$), MET LNs (MET, $n=5$) (**e**), and within the non-tumour area (NT) and tumour area (T) of MET LNs ($n=5$) within 4 h of cell transfer (**f**). **g, h**, The number of adoptively transferred T cells associated with HEVs outside (**g**) and inside (**h**) metastatic lesions, according to the distance from the edge of the lesion. $n=3$. For **b**, statistical analysis was performed using a mixed regression model in which vessel density was the dependent variable identified by individual animals, with the experimental group (non-metastatic TDLN versus metastatic TDLN), time (continuous) and an interaction term between time and group as fixed effects, to show a difference between vessel density in non-metastatic and metastatic TDLNs. For **c** and **e–h**, significance was tested using two-tailed paired Student's *t*-tests (**f–h**) and one-way ANOVA with Tukey's honestly significant difference post hoc test (**c** and **e**). For **e** and **f**, data are mean \pm s.e.m.

LN metastases restrict lymphocyte entry into lesions. To determine whether lymphocyte entry was impaired by remodelled HEVs, we adoptively transferred labelled T cells into mice bearing LN metastases at 5 d (Extended Data Fig. 8), 9 d (Extended Data Fig. 8) and 14 d (Fig. 5d–f) after primary tumour resection. At day 5, metastatic lesions were not well formed. At days 9 and 14, contralateral LN and metastatic LNs showed a higher degree of transferred T-cell accumulation relative to naive LNs (Fig. 5d,e and Extended Data Fig. 8). However, very few transferred T cells entered metastatic lesions within 4 h compared with the adjacent LN tissue (Fig. 5f and Extended Data Fig. 8), suggesting that T cells have limited access

to established lesions within metastatic LNs. Moreover, HEVs deep within metastatic lesions contained fewer T cells than HEVs outside the lesion and those close to the lesion edge (Fig. 5g,h), suggesting that the naive lymphocyte adhesion function was impaired in the few remaining intralymphatic HEVs. Together, these data suggest that the limited number of homeostatic and adoptively transferred T cells that infiltrate metastatic lesions is due to the decreased presence of PNAd⁺ HEVs.

Lesion-specific downregulation of genes associated with lymphocyte trafficking. To determine molecularly how HEV function was

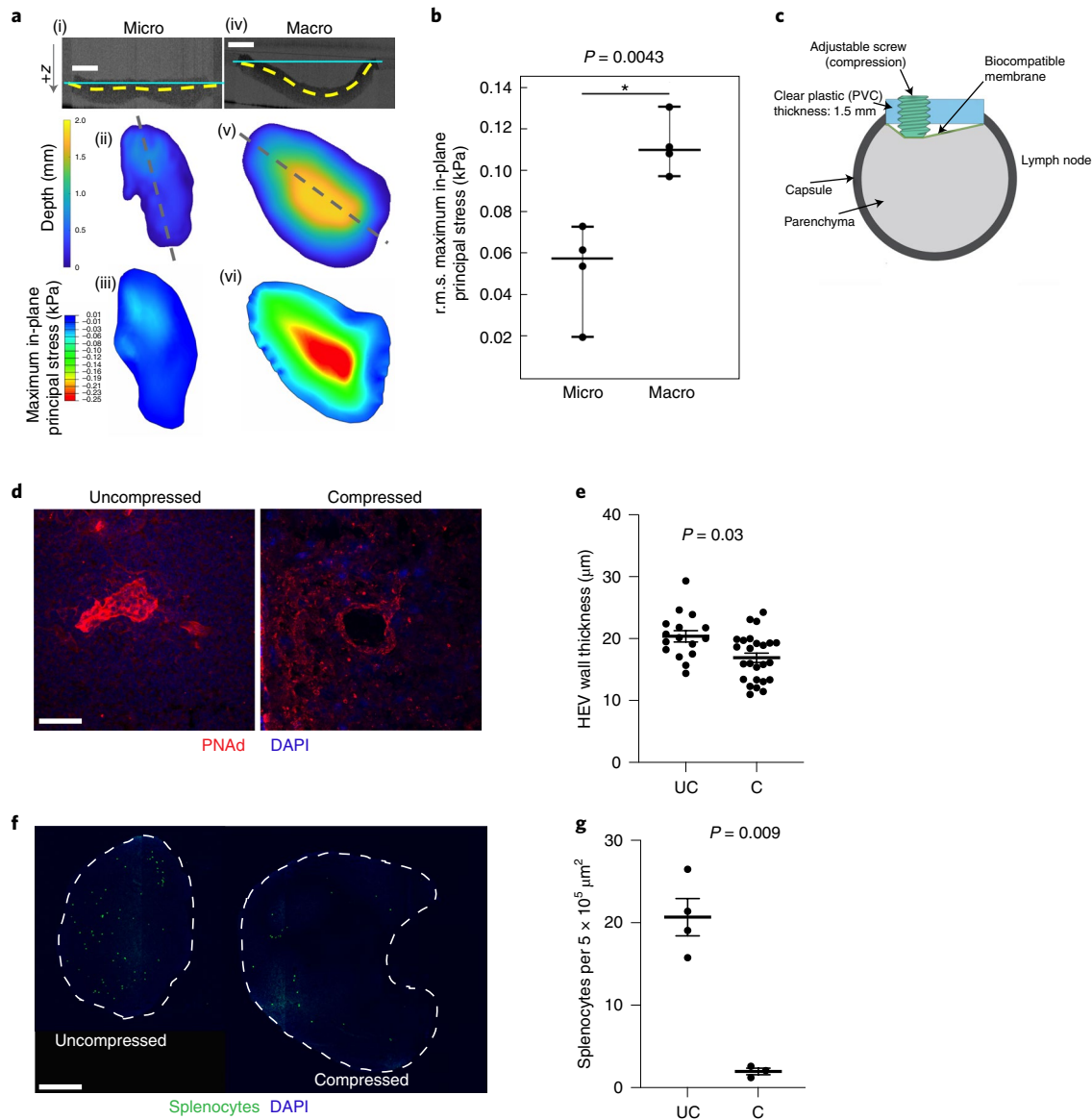


Fig. 6 | Solid stress impairs lymphocyte trafficking into LNs. a, Representative micrometastasis sample (of 4) ((i)–(iii)) and representative macrometastasis sample (of 4) ((iv)–(vi)). Sagittal section of a LN slice from an OCT image stack associated with the grey dashed lines in (ii) and (v) ((i) and (iv)). The yellow dashed line indicates the approximate membrane reconstructed from (ii) and (v). The cyan solid line indicates the zero plane for the OCT image stack for the respective sample. Transverse view of reconstructed membrane profile in MATLAB with a heat map to indicate the distribution of deformation or depth in the z direction ((ii) and (v)). Heat map of the maximum in-plane principal solid stress obtained from the finite-element model of the membrane with deformation described in (ii) and (v) ((iii) and (vi)). Scale bars, 1 mm. **b**, Root mean squared (r.m.s.) maximum in-plane principal solid stress values obtained for all samples in the micrometastasis and macrometastasis groups. $n = 4$. **c**, Schematic of the LN compression device. **d**, Representative IF staining of PNAd⁺ HEVs (red) in an uncompressed (contralateral) and compressed inguinal LN. Scale bar, 40 μm . **e**, Quantification of endothelial wall thickness in uncompressed (UC) and compressed (C) LNs. $n = 3$. **f**, Adoptive transfer of CFSE-labelled (green) naive splenocytes into mice with a compression device. The dashed lines indicate the margin of the LN. Scale bar, 450 μm . **g**, Quantification of adoptively transferred splenocytes entering uncompressed (UC) contralateral LNs ($n = 4$) and compressed (C) inguinal LNs ($n = 3$). For **b**, **e** and **g**, data are median $\pm 1.5 \times$ the respective interquartile range (**b**) and mean \pm s.e.m. (**e** and **g**). Significance was tested using two-tailed unpaired Student's t -tests.

impaired, we isolated tissue from metastatic lesions and adjacent non-metastatic tissue from 4T1 metastatic LNs. As expected, the epithelial marker *Krt18* was enriched in metastatic lesions, but not in adjacent non-tumour tissue (Extended Data Fig. 9a). Compared with non-metastatic tissue, gene expression of *Chst4*, *Fut7*, *Icam1*, *SELP*, *Madcam1* and *Glycam1* (refs. ^{36–39})—which encode molecules that are associated with the PNAd epitope and lymphocyte homing—were reduced in metastatic lesions (Extended Data Fig. 9b–h).

In addition to PNAd, intracellular adhesion molecule-1 (ICAM-1) was significantly reduced within metastatic lesions (Extended Data Fig. 10a–c). Within nodal lesions, the HEV-associated chemokines *Ccl19* and *Ccl21*, which are critical for lymphocyte trafficking and retention in LNs^{40–42}, were also strongly downregulated (Extended Data Fig. 9i,j). Together, these data suggest that the remaining HEVs in metastatic lesions lose their functional ability to recruit lymphocytes.

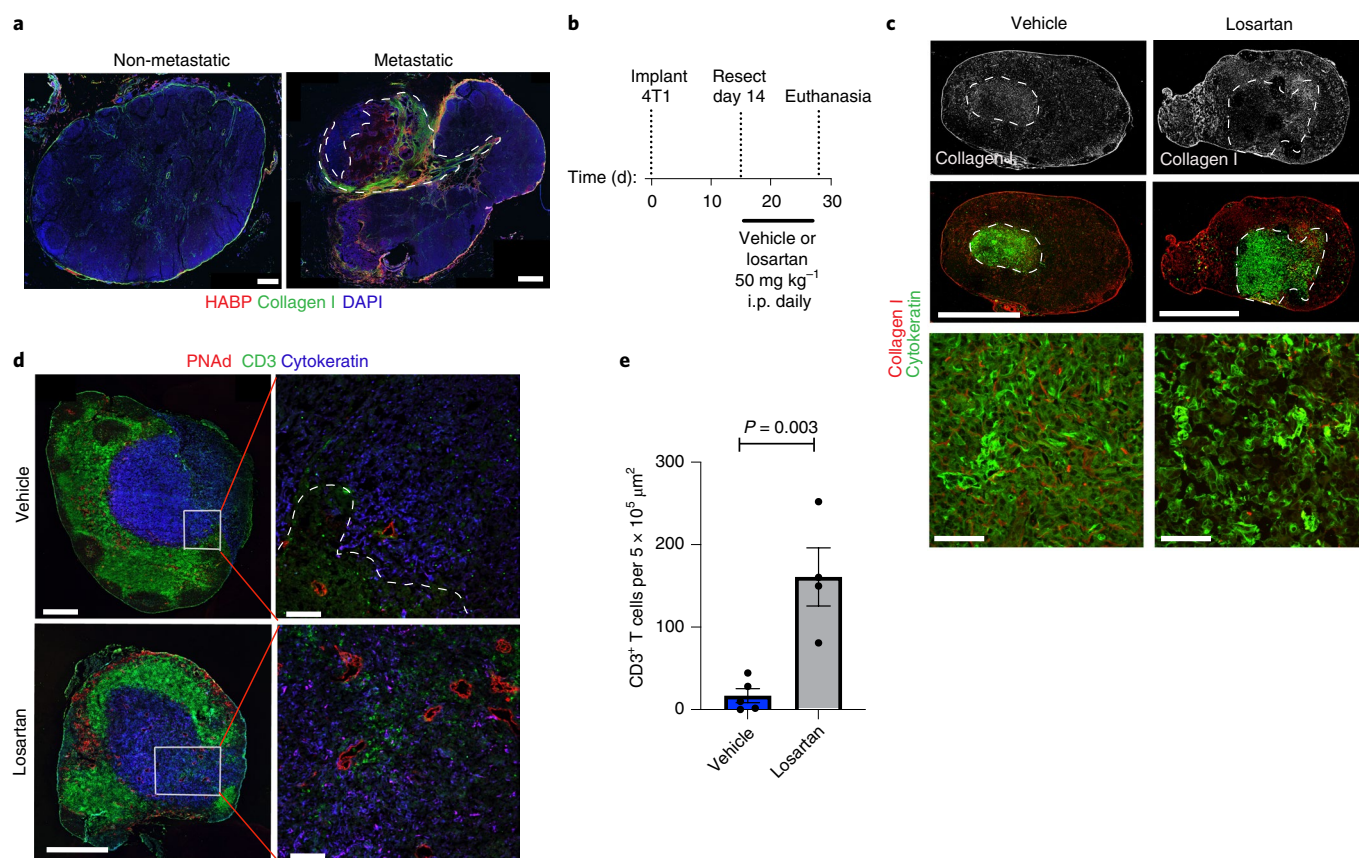


Fig. 7 | Losartan treatment increases T cells within LN lesions. **a**, Representative IF staining ($n = 4$) of collagen I (green) and HABP to detect hyaluronan in LN metastases from patients with breast cancer. Scale bars, 400 μm (non-metastatic) and 600 μm (metastatic). $n = 6$ (non-metastatic); $n = 12$ (metastatic). **b**, Schematic of losartan treatment regimen. **c**, Representative IF staining of collagen I (white, top row; red, middle and bottom rows) and cytokeratin (green) in metastatic LNs from vehicle- and losartan-treated animals. $n = 9$ (vehicle); $n = 4$ (losartan). Scale bars, 636 μm (middle row, which also apply to the top row) and 50 μm (bottom row). Integrated density of collagen 219 a.u. (vehicle), 123 a.u. (losartan). **d**, Representative IF staining of PNA⁺ HEVs (red), CD3⁺ T cells (green) and cytokeratin⁺ cancer cells (blue) in metastatic LNs of BALB/c mice bearing mouse 4T1 cells and treated with vehicle or losartan. Scale bars, 636 μm (left) and 100 μm (right). The number of images taken in **c** and **d** is reflected in the n values for **e**. **e**, Quantification of CD3 T cells depicted in **d**. $n = 5$ (vehicle) and $n = 4$ (losartan). For **a**, **c** and **d**, the dashed lines indicate the margin of the LN lesion. Data are mean \pm s.e.m. Significance was tested using two-tailed unpaired Student's t -tests.

Blood vessel remodelling and impaired lymphocytic trafficking into LN lesions are associated with the presence of solid stress.

On the basis of our previous work showing that solid stress—a compressive mechanical force—can collapse primary tumour vasculature²⁴, we hypothesized that solid stress can collapse intralésion blood vessels, including HEVs, and result in decreased blood perfusion (Fig. 5a–c). Consistent with this hypothesis, we measured a steep decline in the number of HEVs towards the centre of metastatic LN lesions, where the largest solid stress is expected (Fig. 4i–k). We found a trend towards decreased homeostatic T-cell presence as metastatic lesions grew (Extended Data Fig. 9k), which also suggests the functional impairment of HEVs that remain in the lesion trends with increasing solid stress, which we recently measured in metastatic LNs²⁶. Using a tissue-slicing method²⁶, we found greater compressive solid stress in LNs with large metastatic lesions compared to LNs with micrometastasis ($P < 0.05$; Fig. 6a,b), suggesting that the solid stress increases as the lesions grow. Solid stress is concentrated at the centre of the metastatic lesion and dissipates radially outwards, which is physically observed in the deformation of the LN slice (Fig. 6a).

Application of solid stress in LNs phenocopies the effects of solid stress from tumours. To directly determine the effects of

solid stress on vascular collapse and lymphocyte recruitment independent of the presence of cancer, we modified a compression apparatus⁴³ (Fig. 6c) to fit our chronic LN window³⁴. For four consecutive days, we increased the compressive strain at a rate of 0.4 mm d⁻¹ to mimic the gradual increase in solid stress due to tumour growth. Compared with uncompressed LNs, compressed LNs exhibited a significant decrease in HEV wall thickness and diminished PNA⁺ expression (Fig. 6d,e), suggesting a loss of the high-endothelial phenotype. Compared with uncompressed LNs, compressed LNs showed fewer ICAM-1-expressing blood vessels (Extended Data Fig. 10d), although ICAM-1 was expressed on other cellular populations within the LN (Extended Data Fig. 10e). To measure whether compression-induced remodelling influenced lymphocyte trafficking, we adoptively transferred carboxyfluorescein succinimidyl ester (CFSE)-labelled splenocytes, consisting of about 20% T cells (Extended Data Fig. 10f), into animals with compressed LNs. Contralateral LNs showed significantly more infiltrated splenocytes at 4 h after transfer compared with compressed LNs (Fig. 6f,g). Collectively, the compression apparatus reproduces several features of macrometastatic nodal lesions and these data indicate that compressive forces cause the collapse of LN vessels and the reduction of lymphocyte recruitment into LNs.

Reducing solid stress enhances T-cell presence in LN lesions. In addition to cancer cells, the extracellular matrix contributes to solid stress in tumours²³. We measured the extracellular matrix content of LN metastases from patients with breast cancer using IF staining against hyaluronan (by staining hyaluronic acid binding protein (HABP)) and collagen I. LNs with metastases contained more hyaluronan and collagen I compared with non-involved LNs (Fig. 7a). We next investigated the effects of losartan (Fig. 7b), an angiotensin receptor blocker that also has anti-transforming growth factor- β (TGF- β) activity⁴⁴, on the extracellular matrix in metastatic LNs. Losartan has previously been shown to reduce solid stress by reducing collagen in the tumour microenvironment^{45,46}. Treatment of metastatic LNs with losartan after primary tumour removal resulted in reduced collagen within metastatic lesions (Fig. 7c) and increased the presence of HEVs and lymphocytes within LN metastatic lesions (Fig. 7d,e). These data suggest that targeting solid stress using losartan can improve lymphocytic infiltration into LN tumours.

Discussion

Our previous findings show that solid stress in primary tumours can collapse blood and lymphatic vessels²⁴. Reversing this collapse has been shown to lead to increased drug penetration⁴⁶. In this study, data from our longitudinal imaging in metastatic LNs are consistent with vessel collapse. Using a compression apparatus and ex vivo solid stress measurements of metastatic LNs, our results show an association between solid stress and vascular dysfunction in LNs. As most solid tumours will exert a compressive force as they grow, the mechanism that we identified here in models of breast cancer may also be relevant to other cancer types, as suggested by an analysis of samples from patients with breast, colon, and head and neck cancers.

In addition to blood perfusion, blood vessels orchestrate the trafficking of lymphocytes in physiological and disease settings. An effective T-cell-mediated anti-tumour response requires infiltration of T cells into the tumour microenvironment. The presence of ectopic HEVs in human and mouse primary breast cancer is associated with increased T-cell infiltration and is predictive of a favourable prognosis^{47,48}. In LNs, HEVs are critical to ingress of naive lymphocytes. Our data show that solid stress from the growth of metastatic lesions reduces the number of functional HEVs in macrometastatic LN lesions, leading to a lack of lymphocytic infiltration into the lesions. In contrast to previous studies⁴⁹, we did not find HEV remodelling in non-metastatic TDLNs.

Reducing solid stress by decreasing extracellular matrix production, through blocking cancer-associated fibroblast recruitment, has recently been shown to improve drug delivery and increase T-cell infiltration into primary tumours and metastases^{50–52}. Furthermore, the reduction of solid stress improved animal survival when combined with immune checkpoint blockade^{51,52}. The data presented here suggest that reducing solid stress in tumour-involved LNs may promote the normalization of HEVs in LN metastases to enable T-cell entry. Solid stress can be decreased by reducing the extracellular matrix—as demonstrated in this study (Fig. 7)—or by killing cancer cells, as we have shown previously in experimental systems²⁴. Further studies are needed to determine whether the induction of lymphocytic access to metastatic lesions by anti-stromal agents can synergize with immunotherapies such as PD-1/PD-L1 inhibition to induce effective immune responses against LN metastases. Whether reducing solid stress can enhance adoptive cell transfer of tumour-specific lymphocytes or chimeric antigen receptor T cells to eradicate cancer from metastatic lesions and limit their role in cancer progression also requires further investigation.

We cannot rule out secondary effects of solid stress on blood vessels, such as changes in vessel dilation that may influence shear stress on the vessel and T-cell trafficking as a result. Another limitation of our study is that other tumour-induced mechanisms of

T-cell immunosuppression, which probably enable initial metastatic growth, may contribute to the lack of lymphocytic infiltration. Such immunosuppressive mechanisms may remain active in the tumour microenvironment and may limit the activation of infiltrated T cells. Here we show that disruption of IDO and PD-1/PD-L1 signalling did not enhance T-cell activity in LN lesions, but other immunosuppressive mechanisms may be involved. Finally, differences between cancer cell composition and the degree of desmoplasia between tumour types may have a differential impact on vascular function and, therefore, response to anti-fibrotic therapies.

In conclusion, we show that a combination of abnormal lesional vasculature, downregulation of adhesion molecules on endothelial cells and dysregulation of T-cell chemoattractant molecules—which are all driven by compression created by metastatic growth—create immunologically cold LN lesions. Preserving the structure of LNs may improve LN function to enhance tumour-specific T-cell generation and slow or prevent cancer progression.

Methods

Cell lines and animals. We used two different syngeneic breast tumour lines to study the progression of spontaneous metastatic lesions in LNs of BALB/c mice. 4T1 mammary carcinoma (ATCC) and MCA-P1362 (MCA) mammary adenocarcinoma cells (established in the E.L. Steele Laboratories) were grown in vitro in DMEM medium containing 10% fetal bovine serum. Cells were maintained in a 5% CO₂, humidified incubator at 37°C. All cells were recently authenticated and mycoplasma free. 4T1 cells (1–2 × 10⁵) and MCA cells (0.5–1 × 10⁶) in 50 μ l volume of Hanks Balanced Saline Solution were implanted into the second or fourth mammary fat pad of female BALB/c mice (aged 6–10 weeks). Before growing to a maximal size of 10 mm in diameter (approximate tumour volume of 500 mm³), primary tumours were resected. All procedures were performed according to the guidelines of the Institutional Animal Care and Use Committee of the Massachusetts General Hospital and Boston University.

OCT analysis. For OCT, we implanted a chronic LN window^{34,53} 2 d after resection of primary tumours. A custom-built OCT system³⁵ was used to image the structure and vasculature of LNs at intervals of 2 d or 3 d after chronic LN window implantation. Signal processing and volume projection of angiography was performed using custom MATLAB (MathWorks) code (<https://octresearch.org/resources/>).

LN compression device. All materials were purchased from McMaster-Carr unless otherwise stated. The procedure was adapted from a technique for exerting solid stress in mouse brains^{33,54}. A 12.5 mm circular disk with a hole (diameter, 0.5 mm) at the centre was cut from a polyethylene sheet (thickness, 4.5 mm) using a laser cutter with the following settings: 20%/100%/5,000 Hz (speed/power/frequency). The disk was secured with a drill vise and the 0.5-mm-diameter hole was enlarged using a drill press with a drill bit (diameter, 4.2 mm). An M5 tap was used to create screw threads in the 4.2-mm-diameter hole in the disk. A 14-mm circular membrane was cut out of a PVC sheet. A 12.5-mm hole was cut into a 3 cm × 3 cm silicone sheet (thickness, 2 mm) and this hole was used as a holder for the attachment of the PVC membrane to the polyethylene disk. Cyanoacrylate glue was applied to the circumferential edge of the disk, making sure that the glue did not spread to the flat surface of the disk. Once the glue was applied to the edge of the disk, a PVC circular membrane was centred on top of the 12.5-mm hole in the silicone sheet. The disk was centred on top of the membrane. The disk was pushed such that the disk and the PVC membrane below it were squeezed into the 12.5-mm hole in the silicone sheet, securing the membrane to the edges of the disk.

Silicone washers were made by first punching a 1.5-mm hole in the 2-mm-thick silicone sheet. Next, a 3-mm punch was used to cut a disk centred on the first 1.5-mm hole, resulting in a silicone washer. This silicone washer secures the screw in place in the disk to prevent unintended turning. The silicone washer was centred around the threaded hole in the disk on the face opposite the PVC membrane. An 8-mm M5 screw was screwed into the disk until it touched the PVC membrane on the other side.

Statistical methods. Statistical analyses were performed using Prism 7, 8 or 9 (GraphPad), except as noted below. Statistical significance was determined using one-way ANOVA with the Tukey's honestly significant difference post hoc test, two-tailed paired Student's *t*-tests or two-tailed unpaired Student's *t*-tests, as appropriate. Survival curves were calculated using Kaplan–Meier analysis with the non-parametric log-rank test. For incidence of LN metastasis, statistical analysis was performed using a 2 × 2 χ^2 test with Yates correction. To analyse the difference between the relationship of vessel density and time in naive and metastatic LNs (Fig. 5b), we built a mixed regression model in which vessel density was the dependent variable identified by individual animals, with the experimental

group (non-metastatic TDLN versus metastatic TDLN), time (continuous) and an interaction term between time and group as fixed effects. This analysis was performed in Systat12. Statistical significance was set at $P < 0.05$.

Reporting Summary. Further information on research design is available in the Nature Research Reporting Summary linked to this article.

Data availability

The main data supporting the results in this study are available within the paper and its Supplementary Information. The raw and analysed datasets generated during the study are too large to be publicly shared, yet they are available for research purposes from the corresponding authors on reasonable request.

Code availability

Custom MATLAB codes for the signal processing and volume projection of angiography are available online (<https://octresearch.org/resources>). Custom MATLAB code for the analysis of IF stainings is available at Figshare (<https://doi.org/10.6084/m9.figshare.14794827>).

Received: 3 December 2020; Accepted: 17 June 2021;

Published online: 19 July 2021

References

- Jatoi, I., Hilsenbeck, S. G., Clark, G. M. & Osborne, C. K. Significance of axillary lymph node metastasis in primary breast cancer. *J. Clin. Oncol.* **17**, 2334–2340 (1999).
- Ferris, R. L., Lotze, M. T., Leong, S. P., Hoon, D. S. & Morton, D. L. Lymphatics, lymph nodes and the immune system: barriers and gateways for cancer spread. *Clin. Exp. Metastasis* **29**, 729–736 (2012).
- Nathanson, S. D., Kwon, D., Kapke, A., Alford, S. H. & Chitale, D. The role of lymph node metastasis in the systemic dissemination of breast cancer. *Ann. Surg. Oncol.* **16**, 3396–3405 (2009).
- Pereira, E. R. et al. Lymph node metastases can invade local blood vessels, exit the node, and colonize distant organs in mice. *Science* **359**, 1403–1407 (2018).
- Brown, M. et al. Lymph node blood vessels provide exit routes for metastatic tumor cell dissemination in mice. *Science* **359**, 1408–1411 (2018).
- Ubellacker, J. M. et al. Lymph protects metastasizing melanoma cells from ferroptosis. *Nature* **585**, 113–118 (2020).
- Fransen, M. F. et al. Tumor-draining lymph nodes are pivotal in PD-1/PD-L1 checkpoint therapy. *JCI Insight* **3**, e124507 (2018).
- Osorio, J. C. et al. Lesion-level response dynamics to programmed cell death protein (PD-1) blockade. *J. Clin. Oncol.* **37**, 3546–3555 (2019).
- Spitzer, M. H. et al. Systemic immunity is required for effective cancer immunotherapy. *Cell* **168**, 487–502 (2017).
- Allen, B. M. et al. Systemic dysfunction and plasticity of the immune macroenvironment in cancer models. *Nat. Med.* **26**, 1125–1134 (2020).
- Oh, S. et al. PD-L1 expression by dendritic cells is a key regulator of T-cell immunity in cancer. *Nat. Cancer* **1**, 681–691 (2020).
- Wu, T. D. et al. Peripheral T cell expansion predicts tumour infiltration and clinical response. *Nature* **579**, 274–278 (2020).
- Yost, K. E. et al. Clonal replacement of tumor-specific T cells following PD-1 blockade. *Nat. Med.* **25**, 1251–1259 (2019).
- Mani, V. et al. Migratory DCs activate TGF- β to precondition naive CD8⁺ T cells for tissue-resident memory fate. *Science* **366**, eaav5728 (2019).
- Broggi, M. A. S. et al. Tumor-associated factors are enriched in lymphatic exudate compared to plasma in metastatic melanoma patients. *J. Exp. Med.* **216**, 1091–1107 (2019).
- Hirakawa, S. et al. VEGF-C-induced lymphangiogenesis in sentinel lymph nodes promotes tumor metastasis to distant sites. *Blood* **109**, 1010–1017 (2007).
- Mellor, A. L. & Munn, D. H. Creating immune privilege: active local suppression that benefits friends, but protects foes. *Nat. Rev. Immunol.* **8**, 74–80 (2008).
- Jeanbart, L. et al. Enhancing efficacy of anticancer vaccines by targeted delivery to tumor-draining lymph nodes. *Cancer Immunol. Res.* **2**, 436–447 (2014).
- Ma, L. et al. Enhanced CAR-T cell activity against solid tumors by vaccine boosting through the chimeric receptor. *Science* **365**, 162–168 (2019).
- Chang, A. Y. et al. Spatial organization of dendritic cells within tumor draining lymph nodes impacts clinical outcome in breast cancer patients. *J. Transl. Med.* **11**, 242 (2013).
- Nunez, N. G. et al. Tumor invasion in draining lymph nodes is associated with Treg accumulation in breast cancer patients. *Nat. Commun.* **11**, 3272 (2020).
- Polak, M. E. et al. Mechanisms of local immunosuppression in cutaneous melanoma. *Br. J. Cancer* **96**, 1879–1887 (2007).
- Nia, H. T., Munn, L. L. & Jain, R. K. Physical traits of cancer. *Science* **370**, eaaz0868 (2020).
- Padera, T. P. et al. Pathology: cancer cells compress intratumour vessels. *Nature* **427**, 695 (2004).
- Jain, R. K., Martin, J. D. & Stylianopoulos, T. The role of mechanical forces in tumor growth and therapy. *Annu. Rev. Biomed. Eng.* **16**, 321–346 (2014).
- Nia, H. T. et al. Solid stress and elastic energy as measures of tumour mechanopathology. *Nat. Biomed. Eng.* **1**, 0004 (2016).
- Harrell, M. L., Iritani, B. M. & Ruddell, A. Tumor-induced sentinel lymph node lymphangiogenesis and increased lymph flow precede melanoma metastasis. *Am. J. Pathol.* **170**, 774–786 (2007).
- Gu, Y. et al. Tumor-educated B cells selectively promote breast cancer lymph node metastasis by HSPA4-targeting IgG. *Nat. Med.* **25**, 312–322 (2019).
- Diem, S. et al. Tumor infiltrating lymphocytes in lymph node metastases of stage III melanoma correspond to response and survival in nine patients treated with ipilimumab at the time of stage IV disease. *Cancer Immunol. Immunother.* **67**, 39–45 (2018).
- Uyttenhove, C. et al. Evidence for a tumoral immune resistance mechanism based on tryptophan degradation by indoleamine 2,3-dioxygenase. *Nat. Med.* **9**, 1269–1274 (2003).
- Rooney, M. S., Shukla, S. A., Wu, C. J., Getz, G. & Hacohen, N. Molecular and genetic properties of tumors associated with local immune cytolytic activity. *Cell* **160**, 48–61 (2015).
- Spranger, S. et al. Up-regulation of PD-L1, IDO, and T_H17 cells in the melanoma tumor microenvironment is driven by CD8⁺ T cells. *Sci. Transl. Med.* **5**, 200ra116 (2013).
- Ruddle, N. H. High endothelial venules and lymphatic vessels in tertiary lymphoid organs: characteristics, functions, and regulation. *Front. Immunol.* **7**, 491 (2016).
- Jeong, H. S. et al. Investigation of the lack of angiogenesis in the formation of lymph node metastases. *J. Natl. Cancer Inst.* **107**, djv155 (2015).
- Vakoc, B. J. et al. Three-dimensional microscopy of the tumor microenvironment in vivo using optical frequency domain imaging. *Nat. Med.* **15**, 1219–1223 (2009).
- Pablos, J. L. et al. A HEV-restricted sulfotransferase is expressed in rheumatoid arthritis synovium and is induced by lymphotoxin- α/β and TNF- α in cultured endothelial cells. *BMC Immunol.* **6**, 6 (2005).
- Maly, P. et al. The alpha(1,3)fucosyltransferase Fuc-TVII controls leukocyte trafficking through an essential role in L-, E-, and P-selectin ligand biosynthesis. *Cell* **86**, 643–653 (1996).
- Homeister, J. W. et al. The $\alpha(1,3)$ fucosyltransferases FucT-IV and FucT-VII exert collaborative control over selectin-dependent leukocyte recruitment and lymphocyte homing. *Immunity* **15**, 115–126 (2001).
- Tangemann, K., Bistrup, A., Hemmerich, S. & Rosen, S. D. Sulfation of a high endothelial venule-expressed ligand for L-selectin. Effects on tethering and rolling of lymphocytes. *J. Exp. Med.* **190**, 935–942 (1999).
- Gunn, M. D. et al. A chemokine expressed in lymphoid high endothelial venules promotes the adhesion and chemotaxis of naive T lymphocytes. *Proc. Natl. Acad. Sci. USA* **95**, 258–263 (1998).
- Baekkevold, E. S. et al. The CCR7 ligand eIC (CCL19) is transcytosed in high endothelial venules and mediates T cell recruitment. *J. Exp. Med.* **193**, 1105–1112 (2001).
- Drayton, D. L., Liao, S., Mounzer, R. H. & Ruddle, N. H. Lymphoid organ development: from ontogeny to neogenesis. *Nat. Immunol.* **7**, 344–353 (2006).
- Seano, G. et al. Solid stress in brain tumours causes neuronal loss and neurological dysfunction and can be reversed by lithium. *Nat. Biomed. Eng.* **3**, 230–245 (2019).
- Cohn, R. D. et al. Angiotensin II type 1 receptor blockade attenuates TGF- β -induced failure of muscle regeneration in multiple myopathic states. *Nat. Med.* **13**, 204–210 (2007).
- Diop-Frimpong, B., Chauhan, V. P., Krane, S., Boucher, Y. & Jain, R. K. Losartan inhibits collagen I synthesis and improves the distribution and efficacy of nanotherapeutics in tumors. *Proc. Natl. Acad. Sci. USA* **108**, 2909–2914 (2011).
- Chauhan, V. P. et al. Angiotensin inhibition enhances drug delivery and potentiates chemotherapy by decompressing tumour blood vessels. *Nat. Commun.* **4**, 2516 (2013).
- Martinet, L. et al. High endothelial venules (HEVs) in human melanoma lesions: major gateways for tumor-infiltrating lymphocytes. *Oncimmunology* **1**, 829–839 (2012).
- Allen, E. et al. Combined antiangiogenic and anti-PD-L1 therapy stimulates tumor immunity through HEV formation. *Sci. Transl. Med.* **9**, eaak9679 (2017).
- Qian, C. N. et al. Preparing the “soil”: the primary tumor induces vasculature reorganization in the sentinel lymph node before the arrival of metastatic cancer cells. *Cancer Res.* **66**, 10365–10376 (2006).
- Zhao, Y. et al. Losartan treatment enhances chemotherapy efficacy and reduces ascites in ovarian cancer models by normalizing the tumor stroma. *Proc. Natl. Acad. Sci. USA* **116**, 2210–2219 (2019).

51. Chen, I. X. et al. Blocking CXCR4 alleviates desmoplasia, increases T-lymphocyte infiltration, and improves immunotherapy in metastatic breast cancer. *Proc. Natl Acad. Sci. USA* **116**, 4558–4566 (2019).
52. Chauhan, V. P. et al. Reprogramming the microenvironment with tumor-selective angiotensin blockers enhances cancer immunotherapy. *Proc. Natl Acad. Sci. USA* **116**, 10674–10680 (2019).
53. Meijer, E. F. J. et al. Murine chronic lymph node window for longitudinal intravital lymph node imaging. *Nat. Protoc.* **12**, 1513–1520 (2017).
54. Nia, H. T. et al. In vivo compression and imaging in mouse brain to measure the effects of solid stress. *Nat. Protoc.* **15**, 2321–2340 (2020).

Acknowledgements

We thank G. Lauwers, D. Wattson, E. Brachtel and H. Jeong for providing patient samples; M. Erfanzadeh for assistance with MATLAB code optimization for OCT image analysis; and R. K. Jain and J. L. Browning for discussions. This work was supported by the NIH under award numbers R21AI097745, DP2OD008780, R01CA214913 and R01HL128168 (to T.P.P.). Research reported in this publication was supported in part by the Center for Biomedical OCT Research and Translation through grant number P41EB015903, awarded by the National Institute of Biomedical Imaging and Bioengineering of the NIH. This work was supported in part by the National Cancer Institute Federal Share of Proton Income (CA059267, to T.P.P. and B.J.V.), the National Cancer Institute (R01CA163528, to B.J.V.), Massachusetts General Hospital Executive Committee on Research ISF and Research Scholars Program (to T.P.P.), the Johnson and Johnson Cancer Initiative, Boston University Dean's Catalyst Award, and American Cancer Society and Center for Multiscale and Translational Mechanobiology Pilot Grants (H.T.N.). This work was also supported in part by the United Negro College Fund–Merck Science Initiative Postdoctoral Fellowship (to D.J.), the Burroughs Wellcome Fund Postdoctoral Enrichment Program Award (to D.J.), the NIH National Cancer Institute (F32CA183465 and K22CA230315, to D.J.), the American Cancer Society Institutional Research Grant (to D.J.), the METAvivor Early Career Investigator Grant, Shamim and Ashraf Dahod Breast Cancer Research Center (to D.J.), the Boston University Undergraduate Research Opportunities Program (to Z.W.), the NIH National Cancer Institute (K00CA234940, to H.Z.) and the MGH ECOR Fund for Medical Discovery Postdoctoral Fellowship Award (to E.R.P.). This work was conducted with support from

H. Lee of MGH and Harvard Catalyst; the Harvard Clinical and Translational Science Center (National Center for Advancing Translational Sciences, National Institutes of Health Award UL1TR002541); and financial contributions from Harvard University and its affiliated academic healthcare centres. The content is solely the responsibility of the authors and does not necessarily represent the official views of Harvard Catalyst, Harvard University and its affiliated academic healthcare centres, or the National Institutes of Health.

Author contributions

D.J. and T.P.P. conceived and designed the study, analysed data and wrote the manuscript, which all of the co-authors commented on. D.J., Z.W., I.X.C., S.Z., R.B., P.-J.L., V.X., C.K., J.W.M.v.W. and E.R.P. designed and performed experiments and analysed data. H.Z. performed adoptive transfer and losartan experiments. H.T.N. designed the LN compression device and mathematical modelling. P.H. isolated and characterized the MCa-P1362 cell line. B.J.V. contributed to imaging analyses and imaging tools.

Competing interests

The authors declare no competing interests.

Additional information

Extended data is available for this paper at <https://doi.org/10.1038/s41551-021-00766-1>.

Supplementary information The online version contains supplementary material available at <https://doi.org/10.1038/s41551-021-00766-1>.

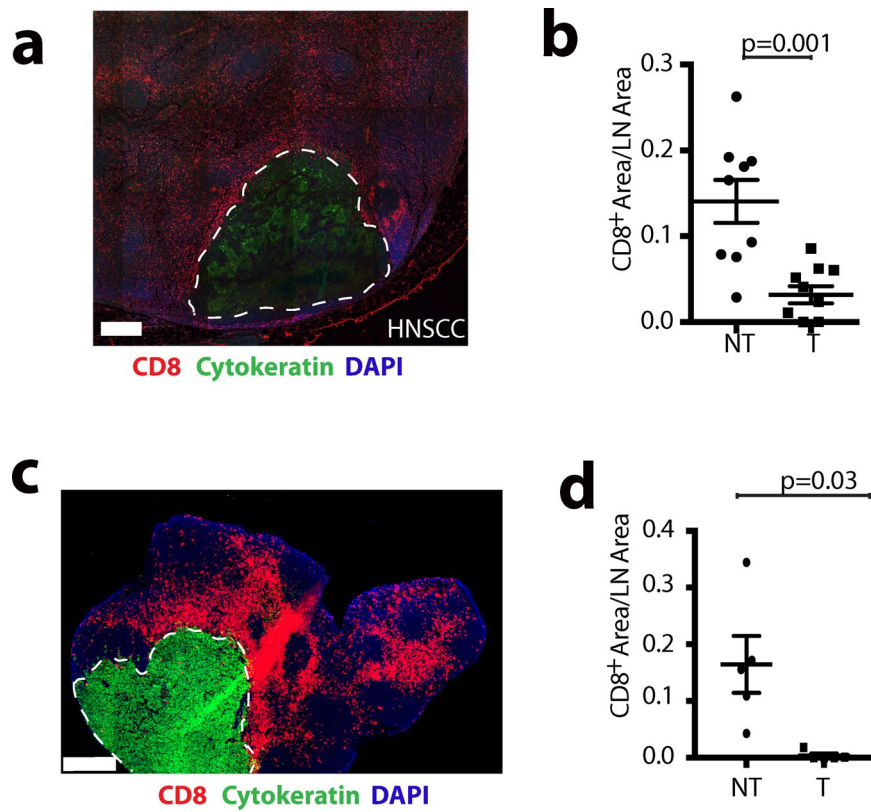
Correspondence and requests for materials should be addressed to D.J. or T.P.P.

Peer review information *Nature Biomedical Engineering* thanks Raffaella Righetti and the other, anonymous, reviewer(s) for their contribution to the peer review of this work. Peer reviewer reports are available.

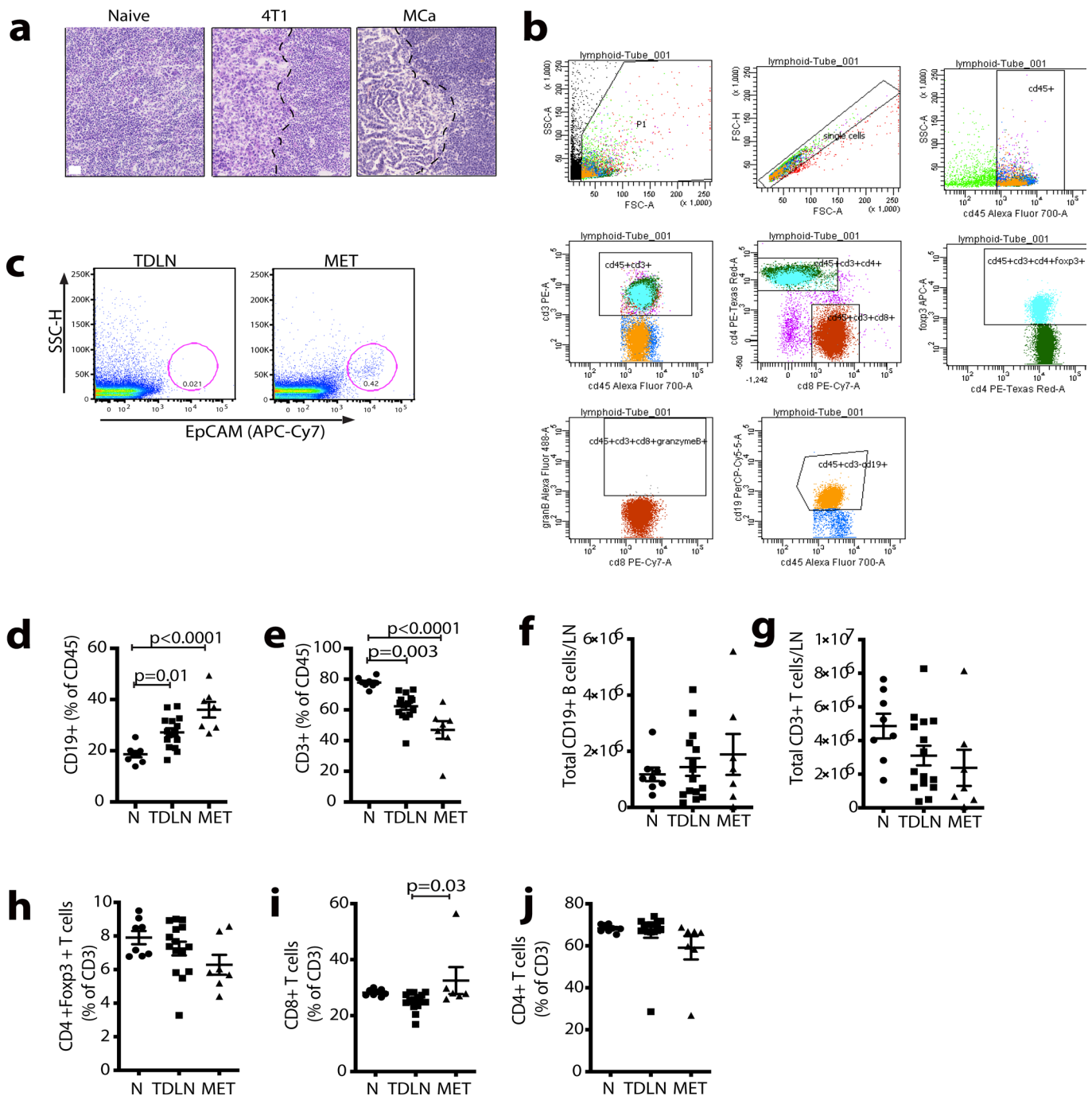
Reprints and permissions information is available at www.nature.com/reprints.

Publisher's note Springer Nature remains neutral with regard to jurisdictional claims in published maps and institutional affiliations.

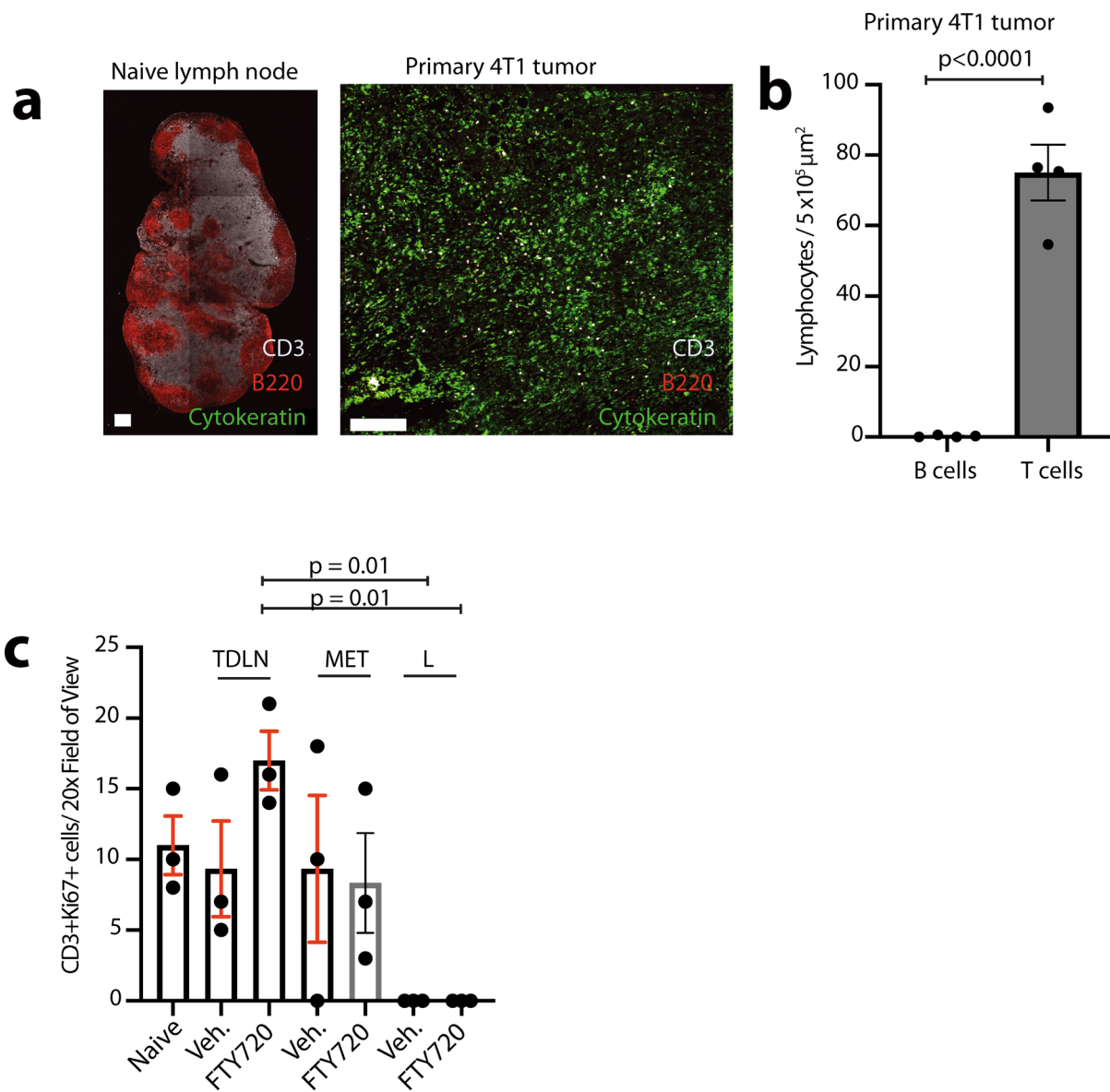
© The Author(s), under exclusive licence to Springer Nature Limited 2021



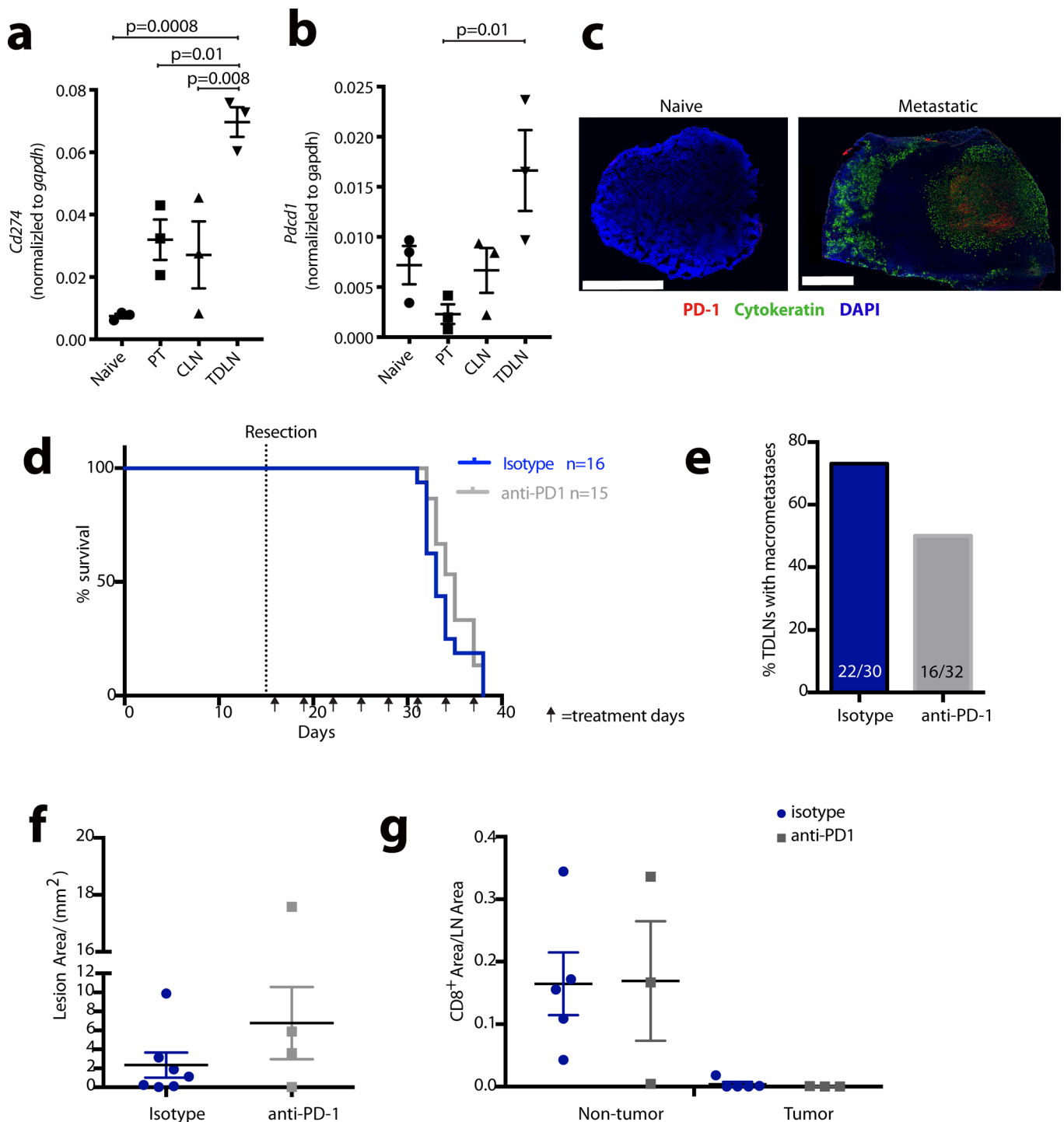
Extended Data Fig. 1 | Lack of CD8 T-cell infiltration into the metastatic lesion. **a**, Representative (out of about 13 images) image of immunofluorescent staining of CD8 T cells (red) in a metastatic lymph node of a patient with head and neck squamous cell carcinoma (HNSCC). Cancer cells were stained with anti-cytokeratin (green). The dashed line indicates the margin of the lymph-node lesion. Scale bar, 636 μm . **b**, Quantification of the area of CD8 T cells within the metastatic tumour (T) and the adjacent non-tumour (NT) lymph-node area in LN-bearing HNSCC ($n=13$). **c**, Representative (out of about 5 images) images of immunofluorescent staining of CD8 T cells (red) in metastatic lymph nodes of mice bearing mouse 4T1 cancer cells. Cancer cells were stained with anti-cytokeratin (green). The dashed line indicates the margin of the lymph-node lesion. Scale bar, 636 μm . **d**, Quantification of the area of CD8 T cells in LNs bearing 4T1 cells within the non-tumour area (NT) and tumour area (T) ($n=5$). Data plotted as mean \pm s.e.m. Statistical significance was tested via a 2-tailed paired Students' *t*-test. DAPI (blue) stains all nucleated cells.



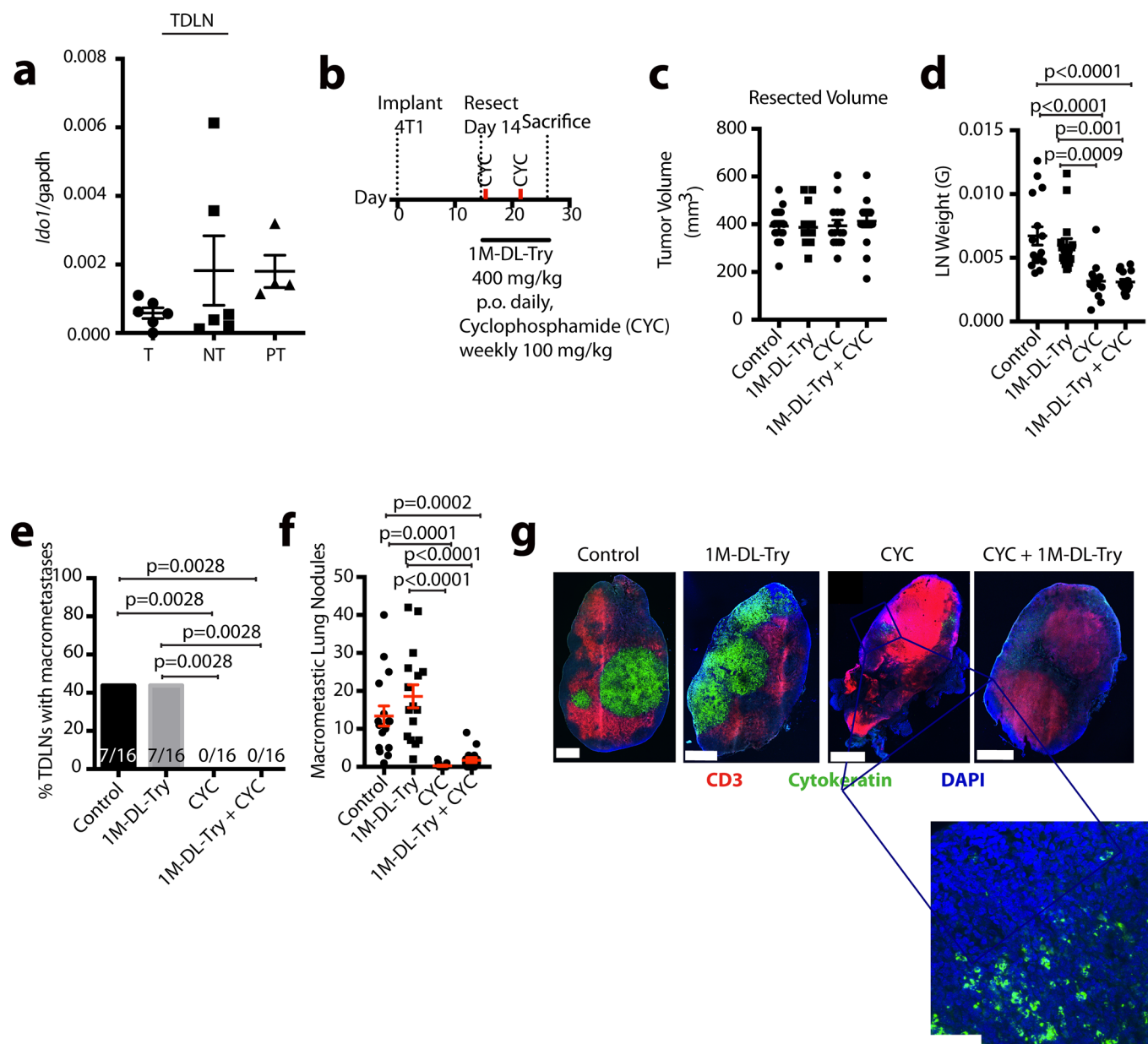
Extended Data Fig. 2 | Quantification of immune populations in tumour draining lymph nodes. **a**, Histology of naïve, metastatic 4T1, and metastatic MCa lymph nodes. The dashed line indicates the margin of the lymph-node lesion. The tumour is left of the dashed lines. Scale bar= 50 μ m. $n=3$. **b**, Single-cell suspensions were generated from naïve lymph nodes or from lymph nodes of tumour-bearing mice on day 28 post-4T1 cancer cell implantation. Gating strategy of flow cytometry in d-j. **c**, Flow-cytometry plot showing the presence of EpCAM+ tumour cells in metastatic tumour draining lymph node (MET), right plot, compared to their absence in non-metastatic tumour draining lymph nodes (TDLN), left plot. The presence or absence of EpCAM+ tumour cells (as depicted in c) was used to define TDLNs and MET LNs in d-j. **d**, Flow-cytometry quantification of B cells (CD45+CD19+); **e**, T cells (CD45+ CD3+) from naïve lymph nodes (N) ($n=8$), non-metastatic TDLNs (TDLN) ($n=15$), and metastatic TDLNs (MET) ($n=7$) of mice harbouring 4T1 tumours. Flow-cytometry quantification of total number of (f) CD45+CD19+ and (g) CD45+ CD3+ cells from N, TDLN and MET lymph nodes. For e and f, the total number of B and T cells, respectively, was calculated by multiplying the % population by the total lymph node cell count. Flow cytometry quantification of h, CD45+ CD3+ CD4+ Foxp3+, i, CD45+ CD3+ CD8+ and j, CD45+ CD3+ CD4+ subpopulations from the, N, TDLN and MET LNs. Statistical analysis: Data plotted as the mean \pm s.e.m. Statistical significance was tested by one-way ANOVA with Tukey's Honestly Significant Difference post-hoc test.



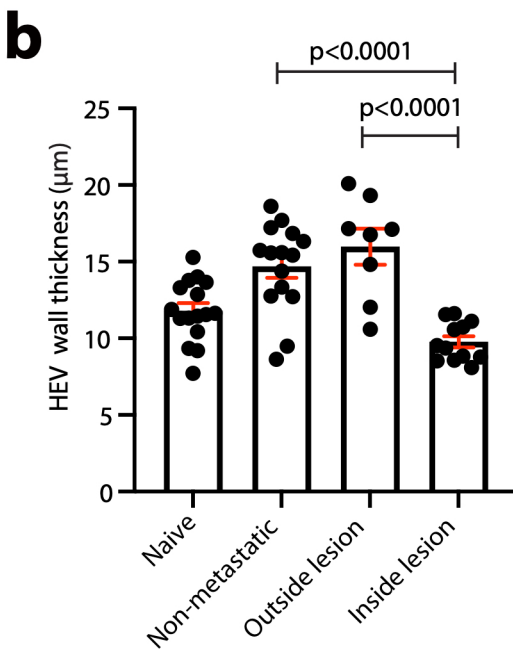
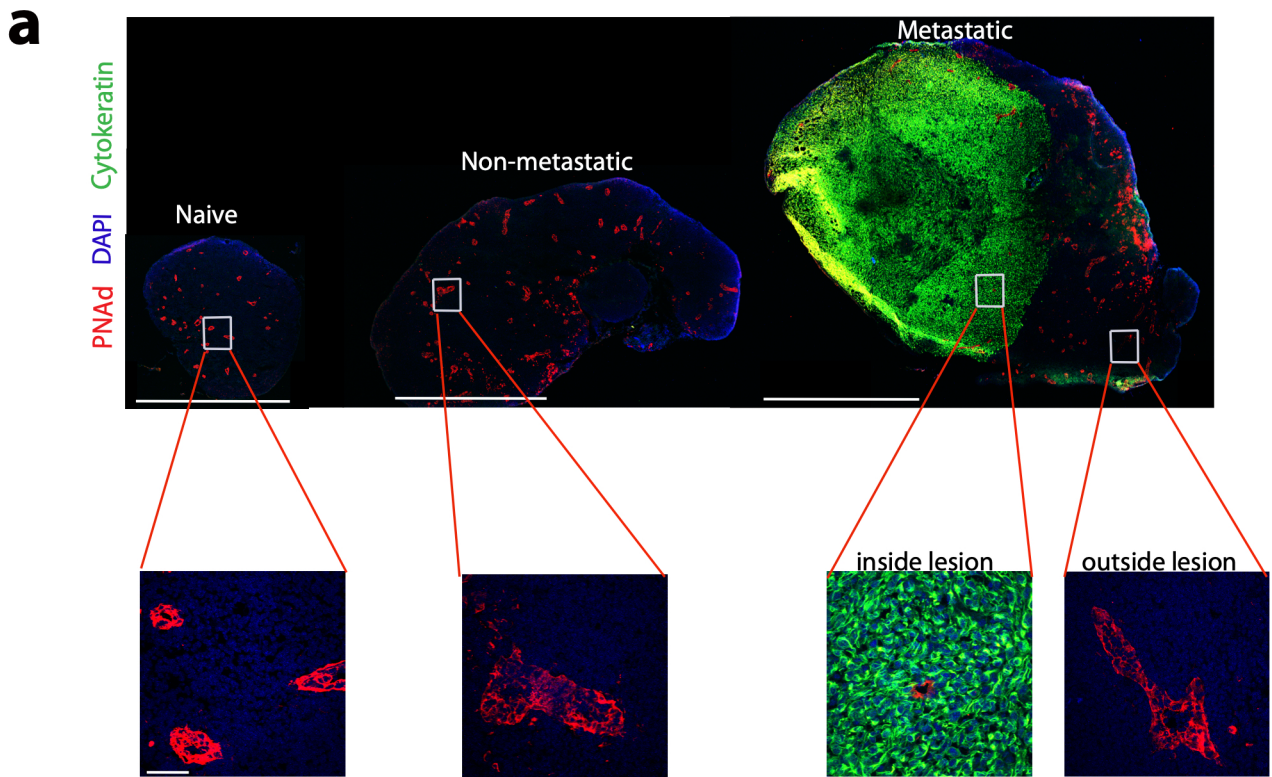
Extended Data Fig. 3 | Analysis of lymphocytes in primary tumours. **a**, Representative immunofluorescent staining of naïve lymph node (positive control, $n = 9$) and 4T1 primary tumour (14 days post-implantation, $n = 4$) stained concomitantly with anti-cytokeratin (green), anti-B220 (red), and anti-CD3 (white). **b**, Quantification of B220 + B cells and CD3 + T cells in 4T1 primary tumours ($n = 4$). **c**, Quantification of proliferating T cells based on CD3 / Ki67 double-positive cells per 20x field of view in FTY720 or control treated mice: TDLN = non-metastatic tumour draining lymph node; MET = LN tissue remaining of a metastatic tumour draining lymph node (outside lesion) and metastatic tissue (inside lesion); L = metastatic lesion only in a metastatic tumour draining lymph node (inside lesion). Statistical analysis: Data plotted as the mean \pm s.e.m. Statistical significance was tested by 2-tailed unpaired Students' t test (b) and by one-way ANOVA with Tukey's Honestly Significant Difference post-hoc test (c).



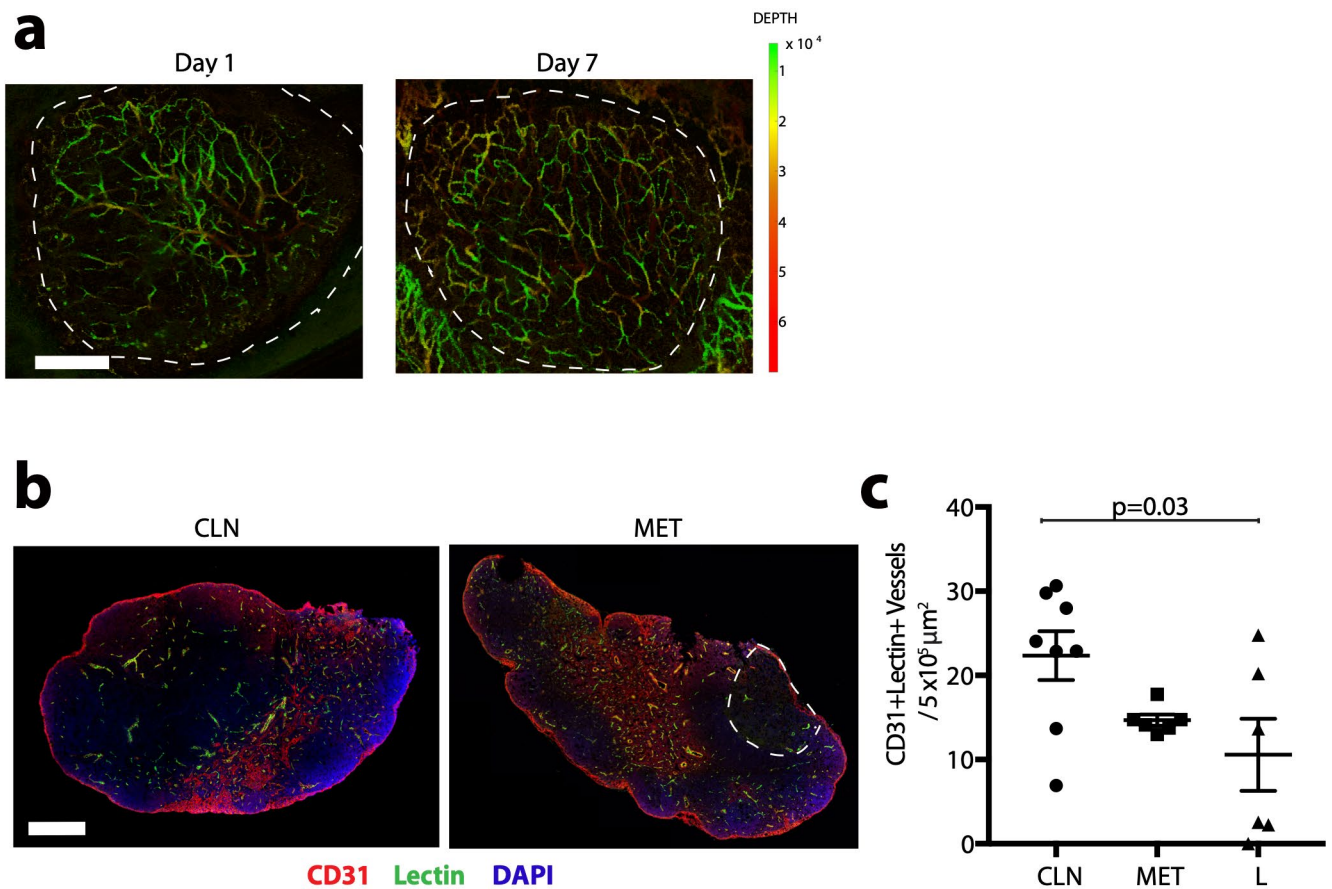
Extended Data Fig. 4 | Effect of anti-PD-1 therapy on lymph node metastasis. Expression of Cd274 (PD-L1) (**a**) and Pdcd1 (PD-1) transcript (**b**) measured by qRT-PCR, in naïve lymph node, primary tumour (PT), contralateral (CLN) and tumour draining lymph nodes (TDLN) from mice bearing 4T1 breast cancer. Relative gene expression calculated using $\Delta\Delta\text{CT}$ method, as normalized against Gapdh ($n=3$ biological replicates for a and b). **c**, Representative immunofluorescent staining (4 images taken from each group) of PD-1+ cells (red) in naïve lymph nodes of Balb/c mice and metastatic lymph nodes from Balb/c mice bearing mouse 4T1 cells. Scale bars = 500 μm . Cancer cells are stained green (cytokeratin+) and DAPI (blue) stains all nucleated cells. **d-e**, 4T1 tumour-bearing Balb/c mice were treated with 200 μg of anti-PD-1 antibody (BioXcell clone RMP1-14, cat# BE0146) or isotype (rat IgG, Jackson ImmunoResearch Laboratories, cat. # 012-000-003) control every 3 days following primary tumour resection 14 days post-implantation. **d**, Survival of animals treated with anti-PD-1 or isotype antibody. Anti-PD-1 $n=15$, isotype; $n=16$. **e**, Incidence of metastatic lymph nodes after anti-PD-1 or isotype antibody treatment, as determined by cytochrome staining of serial lymph node sections. Anti-PD-1 $n=32$, isotype; $n=30$. **f**, Tumour area of cytochrome-positive metastatic lesions after treatment with indicated antibodies. Tumour area was measured using Image J analysis. **g**, Quantification of CD8+ cells within tumour and non-tumour areas of metastatic lymph nodes from 4T1 tumours in Balb/c mice treated with anti-PD-1 antibody or isotype control. Data plotted as the mean \pm s.e.m. Statistical significance was tested by one-way ANOVA with Tukey's Honestly Significant Difference post-hoc test (a-b, f-g). For d, statistical analysis was calculated using Kaplan Meier analysis with non-parametric log-rank test. For e, statistical analysis was performed using a 2×2 chi-square test with Yates correction.



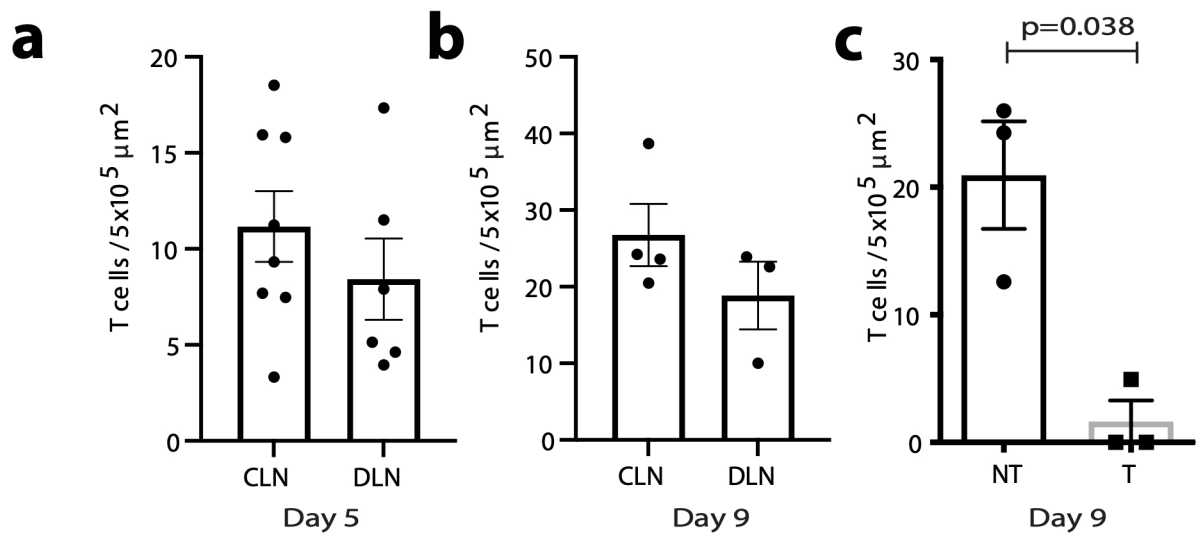
Extended Data Fig. 5 | Effect of IDO inhibition and chemotherapy on lymph-node metastasis. **a**, Expression of *Ido1* measured by qRT-PCR from tumour (T) and non-tumour (NT) regions of metastatic LNs and from primary tumour of mice bearing 4T1 cells (n = 6 biological replicates for tumour and non-tumour, 4 biological replicates for tumour). Relative gene expression normalized to *Gapdh* and calculated using the $2^{-\Delta\Delta CT}$ method. **b**, Schematic of treatment regimen. **c**, Measurement of primary tumour volume at time of resection for each treatment group. **d**, Weight of tumour draining axillary lymph node after treatment. Untreated (n = 16); 1M-DL-Try (n = 16); CYC (cyclophosphamide) (n = 15); 1M-DL-Try + CYC (n = 15). **e**, Incidence of metastatic lymph nodes, as determined by cytokeratin staining of serial lymph node sections. **f**, Quantification of pulmonary macrometastatic nodules after treatment with indicated therapies. Untreated (n = 16); 1M-DL-Try (n = 16); CYC (n = 15); 1M-DL-Try + CYC (n = 16). **g**, Representative immunofluorescent staining of T cells (CD3, red) and cancer cells (cytokeratin, green) in lymph nodes from control (untreated), or treated (as indicated) animals. The inset shows single tumour cells within lymph nodes of cyclophosphamide-treated animals. DAPI (blue) stains all nucleated cells. Scale bars, 500 μm . Inset scale bar = 50 μm . Four images were taken per group. Data plotted as the mean \pm s.e.m. Statistical significance was tested by one-way ANOVA with Tukey's Honestly Significant Difference post-hoc test (c,d,f) and between categorical variables in e using a chi-square test.



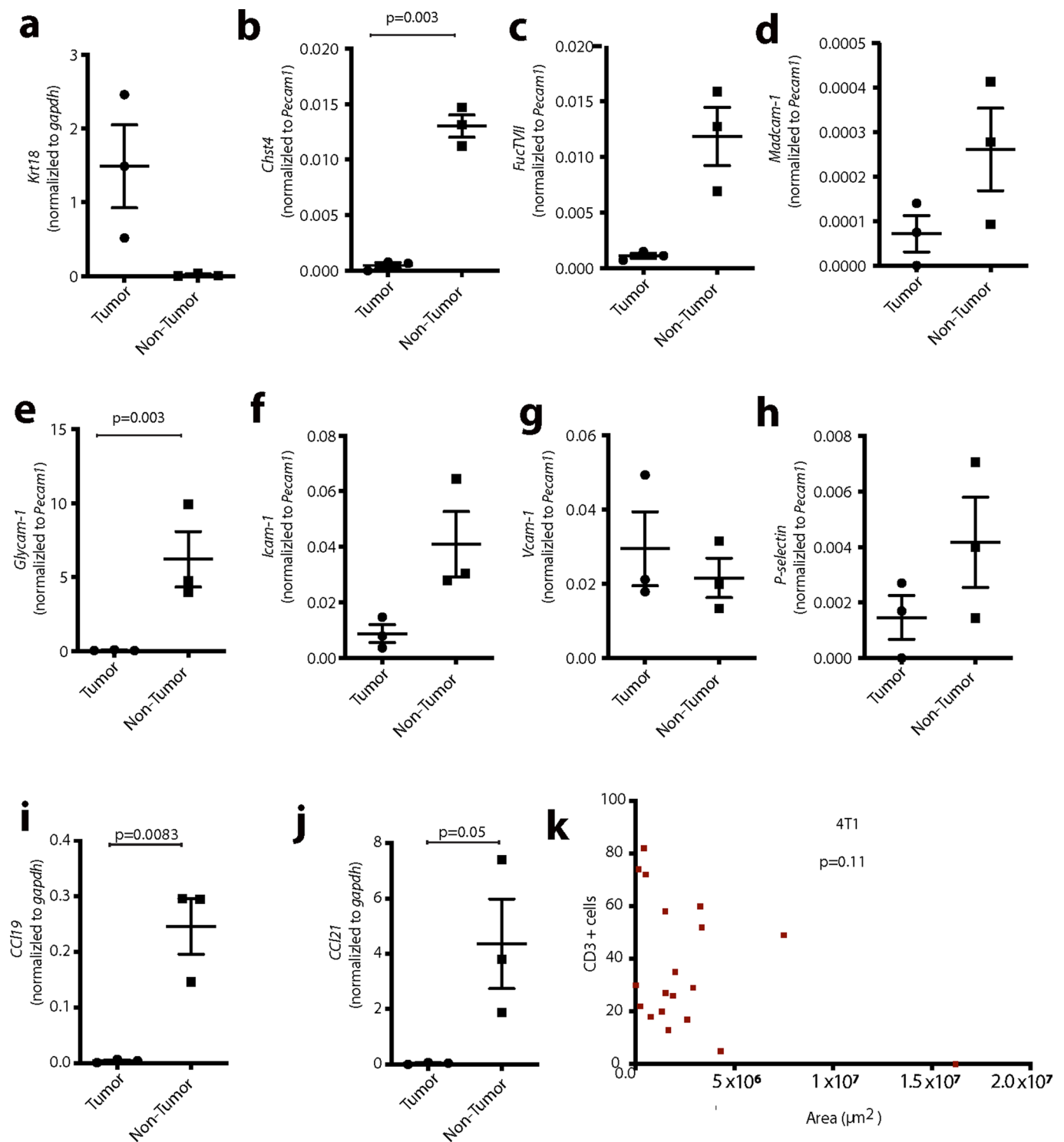
Extended Data Fig. 6 | High-endothelial-venule wall-thickness in non-metastatic and metastatic lymph nodes. **a**, Representative immunofluorescent staining of naïve lymph node, non-metastatic tumour draining lymph node and metastatic tumour draining lymph node with anti-cytokeratin (green) and anti-PNAd (red). DAPI (blue). Scale bars = $1272\mu\text{m}$. Inset below shows magnified region of interest from respective tiled lymph nodes. Scale bar = $50\mu\text{m}$. Four images were taken per group. **b**, Quantification of HEV wall thickness. Each point represents the average of 8 measurements per vessel. $n = 4$ animals for naïve and non-metastatic; $n = 3$ animals for metastatic. Data plotted as mean with 95% CI. Statistical significance was tested by one-way ANOVA with Tukey's Honestly Significant Difference post-hoc test.



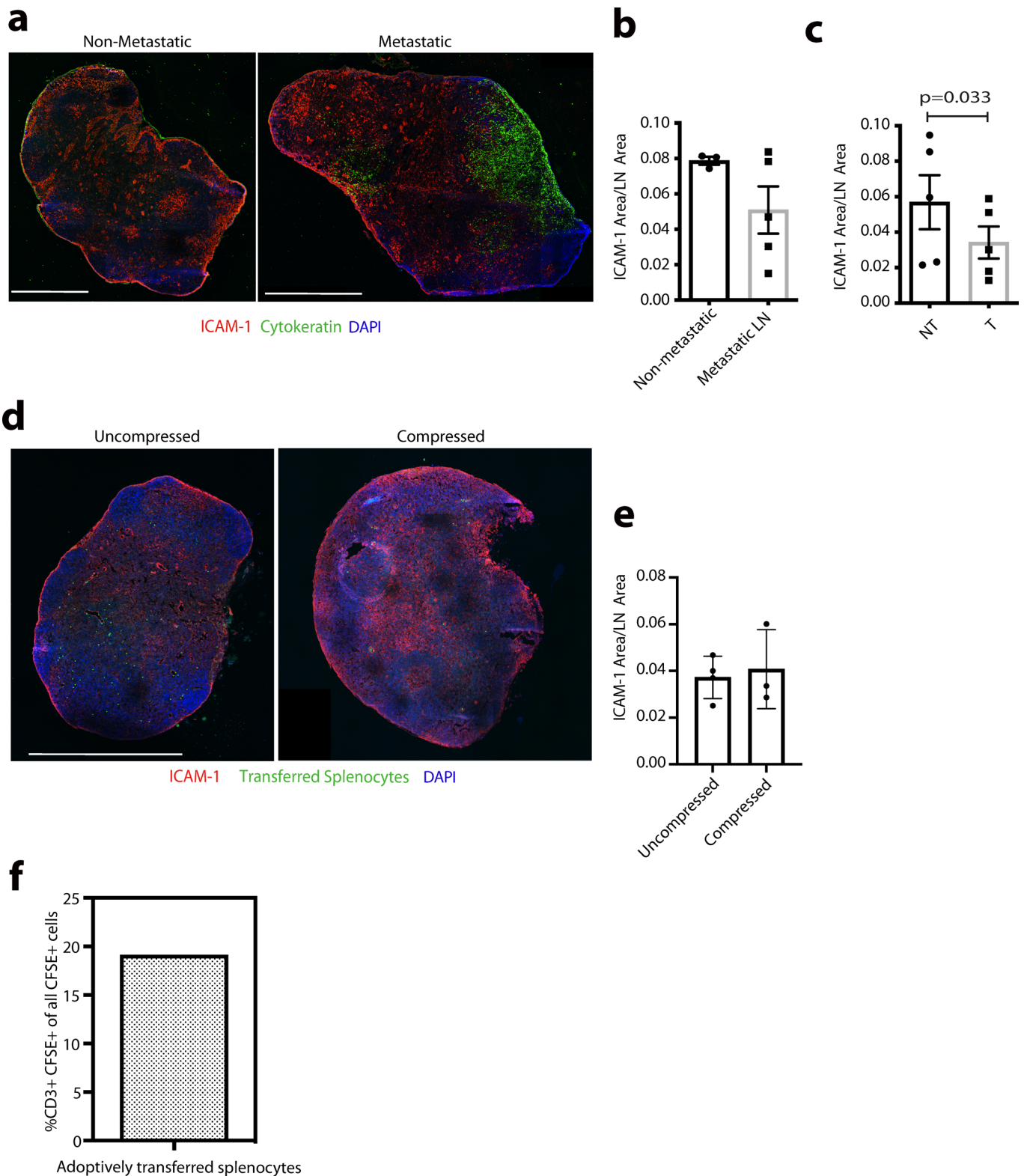
Extended Data Fig. 7 | Vessel perfusion in tumour- draining lymph nodes. **a**, Representative false color OCT non-metastatic TDLN on days 1 and 7 post-primary tumour (4T1) resection. Depth is denoted by color, yellow/green = superficial, red=deep. Dashed line indicates the margin of the lymph node. Scale bar = 500 μm . Experiment is representative of 5 biological replicates. **b**, Representative image of lectin-perfused vessels (green) in contralateral (CLN, left) and metastatic lymph node (MET, right) from animal bearing 4T1 tumour. CD31+ vessels are stained red. Adjacent hematoxylin and eosin-stained sections were used to identify the cancer cell lesion. Dashed line indicates the margin of the lymph node lesion. Scale bar = 500 μm . The number of images taken is reflected in the n values for **c**. **c**, From the 4T1 model, quantification of CD31+ Lectin+ vessels in contralateral lymph nodes (CLNs, $n=8$), metastatic lymph nodes (MET), $n=6$), and only within the lesion (L) of a metastatic lymph node ($n=6$). Data plotted as the mean \pm s.e.m. Statistical significance was tested by one-way ANOVA with Tukey's Honestly Significant Difference post-hoc test.



Extended Data Fig. 8 | Trafficking of adoptively transferred T cells to naïve and tumour draining lymph nodes. Adoptive transfer of CFSE (green)-labeled naïve T cells into naïve or 4T1-tumour bearing mice 5 or 9 days post-primary tumour resection. **a**, Quantification of adoptively transferred T cells (10 million) entering contralateral lymph nodes (CLN) (n=8) and tumour draining lymph nodes (TDLN) (n=6) within 4 hours of cell transfer at Day 5 post-tumour resection. **b**, Quantification of adoptively transferred T cells (14 million) entering contralateral lymph nodes (CLN) (n=4) and tumour draining lymph nodes (TDLN) (n=3) within 4 hours of cell transfer at Day 9 post-tumour resection. **c**, Quantification of the non-tumour area (NT) and tumour area (T) of D9 metastatic LNs (n=3) within 4 hours of cell transfer. Data plotted as the mean \pm s.e.m. Significance tested by one-way ANOVA with Tukey's Honestly Significant Difference post-hoc test (a,b) and 2-tailed paired Students' t-test (c).



Extended Data Fig. 9 | Gene expression in metastatic lymph nodes. **a**, qRT-PCR analysis from tumour (T) and non-tumour (NT) regions of metastatic LNs a, Krt18 was used to confirm the presence of cancer cells in each individual metastatic lymph node. Transcript expression normalized to Gapdh. **b-h**, Analysis of genes related to T cells trafficking. Expression normalized to Pecam1. ($n=3$ biological replicates) **i-j**, Ccl19 (**i**) and Ccl21 (**j**) expression normalized to Gapdh. ($n=3$ biological replicates for both tumour and non-tumour groups in **a-j**). Relative gene expression calculated using $2\Delta\Delta\text{CT}$ method. **k**, Pearson correlation between the number of intralesional CD3+ T cells and lesion area of 4T1 cancer cells in lymph nodes ($r=-0.37$, $n=19$ biological replicates). Data plotted as the mean \pm s.e.m. Statistical significance was tested by 2-tailed paired Students' t -test (**a-j**).



Extended Data Fig. 10 | ICAM-1 in lymph nodes experiencing solid stress. **a**, Representative immunofluorescence staining of ICAM-1 (red) and cytokeratin (green) in non-metastatic and metastatic LNs from mouse 4T1 model. The number of images taken is reflected in the *n* values for **b**. **b**, Quantification of ICAM-1 in non-metastatic (*n* = 3) and metastatic (*n* = 5) lymph nodes. DAPI, blue. **c**, Quantitation of non-tumour area (NT) and tumour area (T) of metastatic LNs (*n* = 5). Scale bars = 636 μ m. **d**, Representative immunofluorescence staining of ICAM-1 (red) in an uncompressed and compressed inguinal lymph node DAPI, blue. Scale bar = 1272 μ m. 3 images were taken per group and are quantified in **e**. **f**, Percentage (of total CFSE + cells) of CD3 + CFSE + cells in animals receiving adoptively transferred splenocytes. *n* = 7 biological replicates. Statistical analysis: Data plotted as the mean \pm s.e.m. Significance tested by 2-tailed unpaired (b,e) and paired Students' *t*-test (c).

Reporting Summary

Nature Portfolio wishes to improve the reproducibility of the work that we publish. This form provides structure for consistency and transparency in reporting. For further information on Nature Portfolio policies, see our [Editorial Policies](#) and the [Editorial Policy Checklist](#).

Statistics

For all statistical analyses, confirm that the following items are present in the figure legend, table legend, main text, or Methods section.

n/a Confirmed

- | | | |
|-------------------------------------|-------------------------------------|--|
| <input type="checkbox"/> | <input checked="" type="checkbox"/> | The exact sample size (n) for each experimental group/condition, given as a discrete number and unit of measurement |
| <input type="checkbox"/> | <input checked="" type="checkbox"/> | A statement on whether measurements were taken from distinct samples or whether the same sample was measured repeatedly |
| <input type="checkbox"/> | <input checked="" type="checkbox"/> | The statistical test(s) used AND whether they are one- or two-sided <i>Only common tests should be described solely by name; describe more complex techniques in the Methods section.</i> |
| <input type="checkbox"/> | <input checked="" type="checkbox"/> | A description of all covariates tested |
| <input type="checkbox"/> | <input checked="" type="checkbox"/> | A description of any assumptions or corrections, such as tests of normality and adjustment for multiple comparisons |
| <input type="checkbox"/> | <input checked="" type="checkbox"/> | A full description of the statistical parameters including central tendency (e.g. means) or other basic estimates (e.g. regression coefficient) AND variation (e.g. standard deviation) or associated estimates of uncertainty (e.g. confidence intervals) |
| <input type="checkbox"/> | <input checked="" type="checkbox"/> | For null hypothesis testing, the test statistic (e.g. F , t , r) with confidence intervals, effect sizes, degrees of freedom and P value noted <i>Give P values as exact values whenever suitable.</i> |
| <input checked="" type="checkbox"/> | <input type="checkbox"/> | For Bayesian analysis, information on the choice of priors and Markov chain Monte Carlo settings |
| <input checked="" type="checkbox"/> | <input type="checkbox"/> | For hierarchical and complex designs, identification of the appropriate level for tests and full reporting of outcomes |
| <input type="checkbox"/> | <input checked="" type="checkbox"/> | Estimates of effect sizes (e.g. Cohen's d , Pearson's r), indicating how they were calculated |

Our web collection on [statistics for biologists](#) contains articles on many of the points above.

Software and code

Policy information about [availability of computer code](#)

Data collection No software was used.

Data analysis Statistical analyses were performed using GraphPad Prism, except for a mixed regression model detailed in the 'Statistical Methods' section of the paper. Flow-cytometry data was analysed using FlowJo. MATLAB or ImageJ were used to quantify lymphocyte populations and blood vasculature in lymph nodes. The algorithm for OCT analysis can be found at <https://octresearch.org/resources>. MATLAB was used for the post-processing of lymph-node-slice deformations, and ABAQUS for the finite-element modelling of solid stress. The MATLAB codes for the signal processing and volume projection of angiography are available from <https://octresearch.org/resources>. The MATLAB code for the analysis of immunofluorescent stainings is available from figshare with the identifier <https://doi.org/10.6084/m9.figshare.14794827>.

For manuscripts utilizing custom algorithms or software that are central to the research but not yet described in published literature, software must be made available to editors and reviewers. We strongly encourage code deposition in a community repository (e.g. GitHub). See the Nature Portfolio [guidelines for submitting code & software](#) for further information.

Data

Policy information about [availability of data](#)

All manuscripts must include a [data availability statement](#). This statement should provide the following information, where applicable:

- Accession codes, unique identifiers, or web links for publicly available datasets
- A description of any restrictions on data availability
- For clinical datasets or third party data, please ensure that the statement adheres to our [policy](#)

The main data supporting the results in this study are available within the paper and its Supplementary Information. The raw and analysed datasets generated during the study are too large to be publicly shared, yet they are available for research purposes from the corresponding authors on reasonable request.

Field-specific reporting

Please select the one below that is the best fit for your research. If you are not sure, read the appropriate sections before making your selection.

- Life sciences Behavioural & social sciences Ecological, evolutionary & environmental sciences

For a reference copy of the document with all sections, see [nature.com/documents/nr-reporting-summary-flat.pdf](https://www.nature.com/documents/nr-reporting-summary-flat.pdf)

Life sciences study design

All studies must disclose on these points even when the disclosure is negative.

| | |
|-----------------|--|
| Sample size | Sample sizes were chosen so as to provide sufficient power for statistical comparisons. |
| Data exclusions | No data were excluded. |
| Replication | All replicates are reported in the manuscript. |
| Randomization | Tumours were grown and resected in an age-matched, size-matched cohort. Mice were randomized with respect to drug treatment. |
| Blinding | The Matlab and Image J analyses of immunofluorescence staining and OCT imaging were done blinded. |

Reporting for specific materials, systems and methods

We require information from authors about some types of materials, experimental systems and methods used in many studies. Here, indicate whether each material, system or method listed is relevant to your study. If you are not sure if a list item applies to your research, read the appropriate section before selecting a response.

Materials & experimental systems

| n/a | Involvement in the study |
|-------------------------------------|---|
| <input type="checkbox"/> | <input checked="" type="checkbox"/> Antibodies |
| <input type="checkbox"/> | <input checked="" type="checkbox"/> Eukaryotic cell lines |
| <input checked="" type="checkbox"/> | <input type="checkbox"/> Palaeontology and archaeology |
| <input type="checkbox"/> | <input checked="" type="checkbox"/> Animals and other organisms |
| <input type="checkbox"/> | <input checked="" type="checkbox"/> Human research participants |
| <input checked="" type="checkbox"/> | <input type="checkbox"/> Clinical data |
| <input checked="" type="checkbox"/> | <input type="checkbox"/> Dual use research of concern |

Methods

| n/a | Involvement in the study |
|-------------------------------------|--|
| <input checked="" type="checkbox"/> | <input type="checkbox"/> ChIP-seq |
| <input type="checkbox"/> | <input checked="" type="checkbox"/> Flow cytometry |
| <input checked="" type="checkbox"/> | <input type="checkbox"/> MRI-based neuroimaging |

Antibodies

| | |
|-----------------|--|
| Antibodies used | Antibody information is detailed in Methods. |
| Validation | Antibodies were validated by the manufacturer. |

Eukaryotic cell lines

Policy information about [cell lines](#)

| | |
|---|--|
| Cell line source(s) | 4T1 cell lines were purchased from ATCC. MCA-P1362 cells were isolated from a spontaneous mammary adenocarcinoma of a Balb/c mouse within the Steele Laboratory animal colony. |
| Authentication | Cell lines were authenticated by submitting samples to Idexx Radil (4011 Discovery Drive, Columbia, MO 65201). Idexx performs the CellCheck 16 Test, which is a genetic 16-Marker STR profile and interspecies contamination test. |
| Mycoplasma contamination | Cell lines were tested for mycoplasma using an ELISA-based assay from Lonza (Mycoalert PLUS Mycoplasma Detection Kit Cat # LT07-710) and a PCR-based assay (PCR Mycoplasma Test Kit I/C, Promokine Cat # PK-CA91-1024). |
| Commonly misidentified lines (See ICLAC register) | No commonly misidentified cell lines were used. |

Animals and other organisms

Policy information about [studies involving animals](#); [ARRIVE guidelines](#) recommended for reporting animal research

| | |
|-------------------------|--|
| Laboratory animals | Tumor studies were initiated on 5–8-week-old female Balb/c mice. All mice were bred and maintained in our Cox-7 gnotobiotic animal colony at Massachusetts General Hospital. |
| Wild animals | The study did not involve wild animals. |
| Field-collected samples | The study did not involve samples collected from the field. |
| Ethics oversight | All procedures were performed following the guidelines of the Institutional Animal Care and Use Committee of the Massachusetts General Hospital and Boston University. |

Note that full information on the approval of the study protocol must also be provided in the manuscript.

Human research participants

Policy information about [studies involving human research participants](#)

| | |
|----------------------------|---|
| Population characteristics | The metastatic lymph nodes from human subjects were de-identified. |
| Recruitment | Not applicable. |
| Ethics oversight | Studies involving human tissues were approved by the Massachusetts General Hospital Institutional Review Board. |

Note that full information on the approval of the study protocol must also be provided in the manuscript.

Flow Cytometry

Plots

Confirm that:

- The axis labels state the marker and fluorochrome used (e.g. CD4-FITC).
- The axis scales are clearly visible. Include numbers along axes only for bottom left plot of group (a 'group' is an analysis of identical markers).
- All plots are contour plots with outliers or pseudocolor plots.
- A numerical value for number of cells or percentage (with statistics) is provided.

Methodology

| | |
|---------------------------|---|
| Sample preparation | Described in Methods. |
| Instrument | LSRII |
| Software | FACSDiva was used for collection, and FlowJo (v10) was used for analysis. |
| Cell population abundance | No cell sorting was performed. |
| Gating strategy | The gating strategy is provided in Extended Fig. 2b. |

- Tick this box to confirm that a figure exemplifying the gating strategy is provided in the Supplementary Information.